Self-Adjusting Imaging Scheme for Ultracold Atoms

Samuel Pinnock

Date: 02.09.2019

A thesis presented for the degree of
Bachelor of Science

Advisor: Prof. Dr. Tilman Pfau

5th Institute of Physics
University of Stuttgart
Germany

Selbst-Justierendes Abbildungssystem für Ultrakalte Atome

Samuel Pinnock

Zusammenfassung

Im Rahmen dieser Bachelorarbeit wird ein Absorptionsabbildungssystem entwickelt, welches in der Lage ist, sich selber nachzuzjustieren. Hierfür muss ein Laserstrahl der gesamten optischen Strecke gerade folgen, was vollkommen von der Ausrichtung eines halben Zollspiegels im gegebenen Ionmikroskop abhängt. Der Spiegel dient dazu, den Laserstrahl, ausgehend von einer Quelle außerhalb des Mikroskops, abzulenken, sodass dieser transversal auf die zu untersuchenden Proben auftrifft. Es besteht jedoch das Problem, dass die Orientierung des Spiegels von Versuch zu Versuch nicht vollständig varriiert. Daher ist es notwendig, dass der optische Aufbau die Richtung vom Laserstrahl korrigieren kann und zwar automatisch. Dies wird ermöglicht, indem ein Testaufbau entwickelt wird, was auf eine teleskopsiche Konfiguration von zwei Sammellinsen basiert. Die Linsekonfiguration sorgt dafür, dass der Laserstrahl stets den gleichen Punkt auf den problematischen Spiegel auftrifft, wobei mittels eines zusätzlichen Spiegels der Einfallswinkel auf den schrägen Spiegel modifiziert wird. Der zusätzliche Spiegel wird in eine drehbare Montage eingebaut, welche mit Motoren getrieben werden kann. Dabei wird ein Mikrokontroller eingesetzt, um die Bewegungen der Montage für den korrigierenden Spiegel mit der gewonnenen Information von einer Quadrantenphotodiode zu koordinieren. Dieser wird gesteuert mithilfe von Software und das Feedback-system für die Motoren beruht auf den gemessenen Ausgangsspannungen der Photodiode, wobei die Position vom Strahl auf der Oberfläche durch Spannungsbedingungen gegeben wird.

Um das Abbildungssystem zu charakterisieren, war es notwendig zu ermitteln, ob die zusätzlich eingebauten Schaltungen für die Photodiode zu Fluktuationen des Nullpunkts der Ausgangsspannungen führten. Darüber hinaus war die Präzession des Korrekturprozesses nach wiederholtem Ausführen festzustellen. Die Fluktuationen wurden mithilfe einer achtstündigen Langzeitmessung untersucht, indem nach jeder Minute ein Bild vom Strahl, zentriert auf der Photodiode, mittels einer CCD-Kamera gemacht und schließlich von jedem Bild die Position auf der CCD-Kamera bestimmt wurde. Demzufolge ließ sich zeigen, dass keine markanten Fluktuationen vorkamen. Danach wurde das Korrektionsprogramm mehrmals für unterschiedliche Winkel des schrägen Spiegels ausgeführt und ein Bild vom Strahl an der Stelle, wo die Atome sich befinden würden, wurde auf die CCD-Kamera abbgebildet. Die Merhheit der Versuche ergaben sich Positionen im Bereich von (200 µm-300 µm), was in Bezug auf die Größe des Strahls ($r \approx 2\,\mathrm{mm}$) und auf die Größe der zukünftigen Atomwolke noch erträglich ist. Soll Vebesserung der Genauigkeit des Korrekturprozesses angestrebt werden, lässt sich diese durch eine Kombination von kleineren Motorschritten und einer verkleinerten Toleranzbedingung erreichen. Schließendlich wurde eine Aufnahme des Strahls während der Nachjustage auf der Photodiode durchgeführt, um zu veranschaulichen, wie das Programm den gesamten Apparatus steuert.

Declaration

Erklärung
Hiermit versichere ich, Samuel Pinnock, Matr.-Nr. 3219283, diese Bachelorarbeit mit dem Titel *Self-Adjusting Imaging Scheme for Ultracold Atoms* eigenständig angefertigt und verfasst zu haben. Es wurden nur die angegebenen Hilfsmittel verwendet. Alle Angaben, die wörtlich oder sinngemäß anderen Werken entnommen wurden, sind unter Angabe der Quelle kenntlich gemacht, wie auch Beiträge anderer Personen. Die Arbeit ist noch nicht veröffentlicht oder in anderer Form als Prüfungsleistung vorgelegt worden.

Contents

List of Figures

Chapter 1

Motivation and Purpose

In the year 1924, the indian physicist, Satyendranath Nath Bose, sent a paper to Albert Einstein called *Quantum Statistics of Light Quanta*. Bose had provided a rederivation of Plank's radiation law without reference to classical mechanics.[3] Einstein promptly translated Bose's work to German, and it was published in the same year. Building on the work of Bose, Einstein contributed a formulation of the statistical distribution of identitical particles with integer spin, now called bosons, and he predicted that if bosonic atoms are cooled to sufficiently low temperatures, they would condense into the lowest possible quantum state, ushering in a new form of matter.[22] In 1938, physicist Fritz London, proposed this so-called Bose-Einstein condensate (BEC) as a mechanism for superfluidity in helium-4 and as a mechanism for superconductivity[14]. The determination to realize this curious new form of matter spurred the development of the field of ultracold atoms with the first BEC in a gas of rubidium atoms evaporatively cooled to 170 nK being produced by Eric Cornell and Carl Wieman at the University of Colorado in 1995, at MIT by the team of Wolfgang Ketterle with sodium atoms, and the group of R. G. Hulet with lithium at Rice University.[2, 4, 5] For the realization of Bose-Einstein condensates, Carl Wieman, Eric Allin, and Wolfgang Ketterle won the Nobel Prize in Physics in 2001.[19]

The persuit to realize Bose-Einstein condensates coincided with the development of novel cooling methods, such as evaporative cooling and laser cooling techniques. The first BECs were realized with a combination of evaporative cooling and magnetic trapping of the atoms, and the first magnetic trap was achieved in 1985 by the group of Alan Migdall.[17] Initial laser cooling techniques were performed on ions which were confined in optical traps using electric fields, and eventually, attempts were made to cool neutral atoms by utilizing a combination of electromagnetic radiation (optical molasses) and magnetic fields.[7] Ultimately, this led to the development of the magneto-optical trap (MOT) and a Nobel Prize in physics for the achievement of laser cooling for Steven Chu, Claude Cohen-Tannoudji, and William D. Phillips.[18] Today, laser cooling and the trapping of atoms are ubiquitous in the field of cold and ultracold atomic physics.

One interesting field within atomic physics is the physics of so-called Rydberg atoms. Rydberg atoms were first observed in plasmas and are readily observable in high-energy environments such as interstellar media in space.[9] One or more electrons in a Rydberg atom possess characteristically high principal quantum numbers n, leading to considerably larger atomic sizes $r \propto n^2$ and electric polarizabilities $\alpha \propto n^7$.[30] Due to this high electric polarizability, the interactions of Rydberg atoms with electric fields and amongst themselves have been the target of research conducted to determine their efficacy as highly sensitive sensors.[20, 25] This, in combination with ultracold quantum gases, has expanded experimental possibilities. For example, Rydberg atoms are said to be frozen (lack thermal mobility) with respect to the time scales of the ultracold experiments, and more recently, the study of Rydberg atoms in vapor cells has also been conducted by using extremely short laser pulses, rendering the atoms essentially motionless during the experiment. This is significant because Rydberg atoms can then be utilized to study dipole-dipole and Van der Waals interactions.[29]

An important tool used to study ultracold atoms and quantum gases are various imaging techniques, such as phase-contrast imaging, flourescence imaging, and absorption imaging. These imaging methods can be deployed to extract characteristics such as temperature, momentum distributions, and information about the spatial distribution of the atoms.[27] Within the scope of this thesis, a self-adjusting absorption imaging scheme is developed. The apparatus will be deployed on an ultracold atomic physics experiment which will optically image the atoms on the vertical axis through an ion microscope. The ion microscope used to detect ions during the experiment is shown in figure 1.1. During the illumination of the atomic cloud, the laser beam is shot into the microscope in which a movable mirror deflects the beam down onto the atomic sample. However, due to the mirrors mobility, the orientation of the mirror is not reproducible and varies slighty each time the mirror is driven into place. Subsequently, the laser beam path through the microscope is suboptimal, if not entirely inhibited. Therefore, the imaging scheme was constructed to be able to automatically modify the direction of the laser beam striking the mobile mirror based on positive feedback obtained from a quad segment photodiode. This ensures that the laser beam travels optimally through the ion microscope to perform the absorption imaging of the atoms, irregardless of the tilt of the mirror.

This thesis is structured in five chapters. The first and second chapters introduce the motivation and theoretical background of the imaging scheme, with emphasis given to geometric optics and the necessary electronic components. The third chapter qualifies and outlines the approach and realization of the imaging scheme with the fourth chapter characterizing the fidelity of the apparatus. Finally, the fifth chapter summarizes this work and presents the future of the imaging scheme and its future utility.

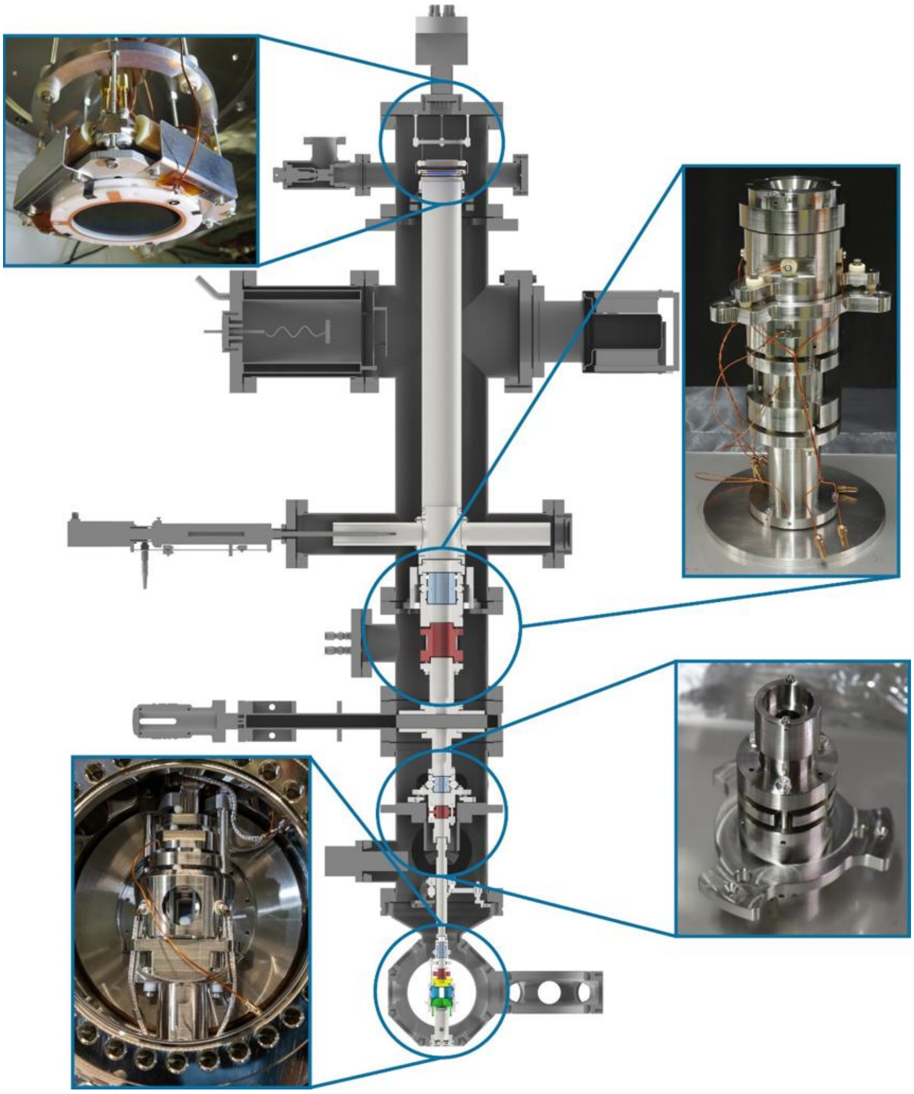

Figure 1.1: Image of the ion microscope employed for the detection of ions in ultracold atom experiments.

Chapter 2

Theoretical Introduction

Although the purpose of the self-adjusting imaging scheme is for absorption imaging, the entire configuration is predicated on optical components whose functionality is described within the regime of geometric optics. The telescopic configuration of the optical set-up used to correct for the unpredictable tilt of the mirror inside the ion microcope can be quantitatively understood through the use of so-called ray transfer matrices. Moreover, because the mirror correcting apparatus is to be automated, the utility of quad segment photodiodes in conjunction with operational amplifiers for the sensing of the laser light becomes relevant.

2.1 Absorption Imaging

Absorption imaging techniques are ubiquitous in the field of ultracold atomic physics. The measuring of the attenuation of the intensity of a laser beam passing through atomic clouds provides information such as the spatial distribution of the atoms, approximation of the atomic column density or the temperature of ultracold quantum gases.

In the case of low atomic densities, the absorption imaging of an ultracold atomic cloud is performed by the illumination of the the cloud with a resonant laser beam [27]. The absorption and scattering of the photons by the electrons of the atoms manifests itself as a reduction in the intensity of the light which is then imaged onto a CCD camera. In order to sufficiently converge the light onto the CCD camera, telescopic lens configurations are typically implemented. Assuming that the incident intensity I_0 of the resonant laser beam is well below the saturation intensity I_{sat} of the atomic transisition under consideration, the attenuation I/I_0 of the laser intensity depends on the initial intensity I_0 of the light, and the absorption coefficient $\kappa(\omega)$[7]:

$$\frac{I}{I_0} = \exp\left[-\kappa(\omega)x\right]. \tag{2.1}$$

In this case, the intensity decreases exponentially with distance x in the absorptive medium, and the absorption coefficient $\kappa(\omega)$ is proportional to the probability of absorption $\sigma(\omega)$ occurring as well as the density of atoms present with which photons can interact n[7]:

$$\kappa(\omega) = n\sigma(\omega). \tag{2.2}$$

$\sigma(\omega)$ is known as the optical absorption cross section and is a parameter which describes the probability of the absorption of a photon by an atom. In the case of low intensity light relative to the saturation intensity, equation 2.2 may be substituted into equation (2.1) yielding:

$$\frac{I}{I_0} = \exp\left[-n\sigma(\omega)x\right]. \tag{2.3}$$

However, in the presence of relatively high intensity, the populations of the atomic levels are affected to a larger extent, with the subsequent stimulated emission contributing to a gain in intensity. This amplification offsets a portion of the absorption and invalidates equation 2.3. If the intensity I is sufficiently large relative to the saturation intensity defined as:

$$I_{\text{sat}} = \frac{\hbar\omega A_{21}}{2\sigma(\omega)}, \tag{2.4}$$

with $\hbar$ being the reduced Plank constanct, ω being the angular frequency of the incident photons and A_{21} describing the rate of spontaneous emission, then the extinction coefficient becomes:

$$\kappa(\omega) = \frac{N\sigma(\omega)}{1 + \frac{I}{I_{\text{sat}}}}. \tag{2.5}$$

Typically, when performing absorption imaging three separate images are taken with the CCD camera: one image in the absence of the atomic cloud, one image with the atoms present, and a final image in the absence of both the illumination laser and the atoms. The third image is used to establish a datum for the other two images.[10]

2.2 Geometric Optics

Geometric optics is founded on three fundamental axioms which are both predicted theoretically and confirmed experimentally. The first axiom is that light rays located in homogenous media can be approximated as straight lines which travel between two points using the minimal distance necessary. The second axiom of geometric optics concerns itself with the behavior of light at the interface between two media with varying permittivities and as a consequence varying refractive indices. According to the law of reflection, the angle of incidence of a light ray at the interface is identical to the angle of reflection. The angle of refraction in the case of transmission between the two media is similarly described by Snell's Law. The third axiom of geometric optics states that the interaction between two light ray bundles which intersect or otherwise converge is negligable with respect to linear optical phenomena. Two convergent light rays may exhibit interference patterns, but the extent of interference is confined to the location of convergence and does not alter the behavior of the light rays when they are seperated [6].

■ Lenses

A lens is an optical device which converges or diverges a light beam by means of refraction. A simple lens is comprised of a single piece of transparent, polished material with a refractive index which is surrounded by a medium of differing refractive index. The various types of optical lenses are characterized by their radii of curvature of the surrounding surface areas. If it is assumed that a light ray is incident from the left of the lens, then the radius of curvature is positive in the case that the midpoint of curvature is on the opposite side to the light source, whereas the radius of curvature is negative when the midpoint lies on the same side as the light source. A lens is classified as convex when the lens itself sits between the midpoint of curvature and the curved surface. In all other cases, the lens is classified as concave. An important characteristic of a lens is the focal point, which is defined as the point at which collimated light rays converge after passing through a lens with a given radius of curvature.[6]

Consider the collimated light ray with a distance h above the optical axis in figure 2.1. The beam passes the spherical surface from the left in a medium with refractive index n_1 and is refracted according to Snell's Law in such a way that the beam intersects with the focal

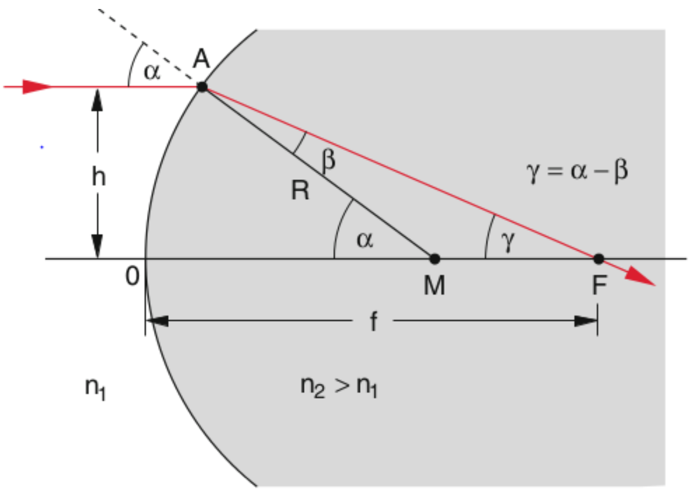

Figure 2.1: Illustration of the refraction of a collimated beam at a spherically curved surface seperating two media with refractive indices n_1 and n_2 with $n_2 > n_1$. [6]

point F. By means of simple geometric consideration, the distance h is approximately given, in the case of a paraxial ray, by the expression:

$$h = R\sin(\alpha) \approx f\sin(\gamma), \tag{2.6}$$

Because the angle γ is equal to the difference of the angles α and β, the focal length f can be expressed as:

$$f = \frac{\sin(\alpha)}{\sin(\alpha-\beta)}R, \tag{2.7}$$

which can further be manipulated by inputing Snell's Law $n_1\sin(\alpha) = n_2\sin(\beta)$ and the trigonometric identity $\sin(\alpha-\beta) = \sin(\alpha)\cos(\beta) - \cos(\alpha)\sin(\beta)$ yielding a relationship between the focal length f and the refractive index n_2:

$$f = \frac{n_2}{n_2\cos(\beta) - n_1\cos(\alpha)}R. \tag{2.8}$$

In the so-called paraxial approximation, it is assumed that the ray makes a small angle α to the optical axis.[23] This allows the cosine terms in equation (2.8) to be Taylor expanded to first order which further simplifies the expression for the focal length f to:

$$f = \frac{n_2}{n_2 - n_1}R. \tag{2.9}$$

Consider now the case of a thin lens with radii of curvature R_1 and R_2. A thin lens is an idealized lens with characteristically minimal distance between the two curved surfaces with respect to the focal lengths f_i.[6] In contrast to the situation above where the light ray is only refracted on one spherically curved surface, a lens presents the situation of two curved surfaces through which the light ray must traverse. This leads to a second refraction of the light ray and subsequent shifting of the image with relative to the location of the image in the case of only one refraction. Quantitatively, this problem is approached by initially disregarding the second surface, determining the point at which the initial image appears, and then considering this image as the object of the second surface for determining the actually observed image. The equation for the observed image B produced by the second refraction can be shown to be equal to:[6]

$$\frac{1}{a} + \frac{1}{b} = (n_2 - 1)\left(\frac{1}{R_1} - \frac{1}{R_2}\right). \tag{2.10}$$

This is significant because the refraction on both curved surfaces of the lens would normally have to be considered when constructing a map of the light rays which would lead to a more complicated equation above. However, due to the approximations allowed by the assumption that the thickness d of the lens is small relative to the distance of the object a and image b, a light ray need only be refracted once on the middle plane of the lens.[6]

Now, determining the focal length from equation (2.10) is possible if considering a parallel light ray from an object effectively an infinite distance away $a = \infty$ and the fact that the ray must pass through the focal point of the lens F. This implies that the image distance must be equal to the focal length $b = f$ and equation (2.10) becomes:

$$f = \frac{1}{n_1 - 1}\left(\frac{R_1 R_2}{R_2 - R_1}\right). \tag{2.11}$$

Plugging this equation (2.11) back into equation (2.10) yields the thin lens equation:

$$\frac{1}{a} + \frac{1}{b} = \frac{1}{f}. \tag{2.12}$$

Quantitatively and qualitatively, contructing an image in the case of geometric optics requires the drawing of only three light rays, which originate from one point on the object.[23] The rays are depicted in figure 2.2. The first light ray, parallel to the optical axis and incident on the lens, intersects with the focal point on the side of the lens where the image appears F_2. The second light ray interects with the focal point on the side of the object F_1, and the third light ray passes through the center of the lens. Generally speaking, the ray passing through the center of the lens is refracted twice in such a way that it is as if the ray were not refracted, merely shifted by a distance Δ proportional to the thickness d of the lens.[6] In the case of a thin lens, however, d tends to zero, and the shift of the ray through the lens may be disregarded.

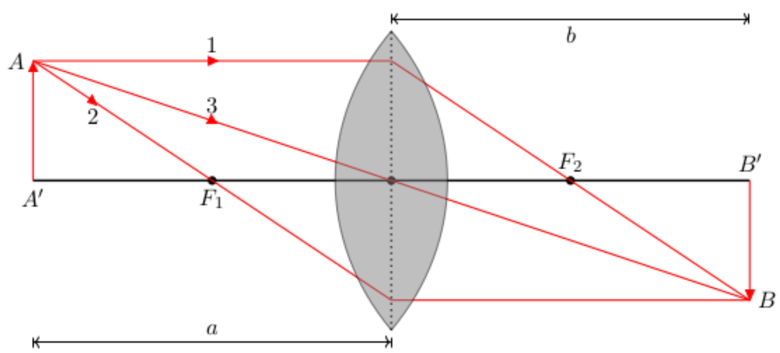

Figure 2.2: Illustration of the construction of an image produced by light passing through a thin lens. The first ray remains parallel to the optical axis before being refracted into the focal point of the lens on the side of the image F_2. The second ray intersects with the focal point of the lens on the side of the object F_1, and The third ray passes through the center of the lens unperturbed.

How the image of the object appears depends on the distance of the object away from the focal point of the lens F_1. The magnification m of the image is defined as the ratio of the line segment $\overline{BB'}$ to the line segment $\overline{AA'}$, both of which are illustrated in figure 2.2. This ratio can be expressed in terms of the distances a and b as well as the focal length of the lens f:[6]

$$m = \frac{\overline{BB'}}{\overline{AA'}} = -\frac{b}{a} = \frac{f}{f - a}. \tag{2.13}$$

If m is negative, then it is implied that the image is inversely oriented with respect to the object. If m is a positive value, then the converse is true; the image and the object have the same orientation. Furthermore, from equation (2.13) it can be deduced that when the object distance a is larger than a focal length $f > 0$, the magnification is always negative, and in the case that $a = 2f$, the object and image are the same size.

■ ABCD-Matrices

When approaching problems in geometric optics concerning several optical components, it can be practicle to introduce a mathematical approach which avoids the necessity to construct arduous ray diagramms. The complexity of dealing with lens systems, for example, can be circumvented to a certain extent by introducing ray transfer matrix formalism. In the so-called ray transfer matrix analysis, light rays are described by vectors consisting of a translational component r and, in the paraxial limit, an angular component $\sin\alpha \approx \alpha$. Optical components such as lenses and mirrors are then described by 2×2 matrices acting on the ray vectors. This makes tracking the behavior of a light ray passing through an optical set-up simpler to follow and predict. The ray transfer method is predicated on two reference planes, the input plane and the output plane. Both the input and output planes are orthogonal to the optical axis, which corresponds to the path taken by a central ray through the system. The input ray vector lies on the input plane before passing an optical component $\nu_1 = (r_1,\alpha_1)^\top$ and the output vector of the outgoing ray $\nu_2 = (r_2,\alpha_2)^\top$ lies on the output plane. [6, 23]

The translational component r of the two dimensional ray vector is given by the distance away from the optical axis of the system, and the angle α is the angle the ray makes with the optical axis. Computing the ray vector in the output plane becomes simple multiplication between an input vector from the input plane and the matrix $\underline{\underline{\boldsymbol{M}}}$ corresponding to the optical component[6]:

$$\begin{pmatrix} r_2 \\ \alpha_2 \end{pmatrix} = \begin{pmatrix} M_{11} & M_{12} \\ M_{21} & M_{22} \end{pmatrix} \begin{pmatrix} r_1 \\ \alpha_1 \end{pmatrix}. \tag{2.14}$$

In order to determine the components of $\underline{\underline{\boldsymbol{M}}}$, the behavior of the light ray before and after passing the component must be considered. For example, the case of a simple translation by a given distance s means that the vector component on the input plane r_1 must become $r_2 = r_1 + s\alpha_1$ on the output plane and the angle α_1 remains the same; therefore, α_2 must equal α_1. Plugging these considerations into the equation (2.14) leads to a system of equations for the individual components of the translation matrix $\underline{\underline{\boldsymbol{T}}}$:

$$\begin{pmatrix} r_1 + s\alpha_1 \\ \alpha_1 \end{pmatrix} = \begin{pmatrix} T_{11} & T_{12} \\ T_{21} & T_{22} \end{pmatrix} \begin{pmatrix} r_1 \\ \alpha_1 \end{pmatrix}. \tag{2.15}$$

Equation (2.15) is only true if $T_{11} = 1$, $T_{12} = s$, $T_{21} = 0$ and $T_{22} = 1$. This yields the definition of the translation matrix $\underline{\underline{\boldsymbol{T}}}$ in the ray transfer formalism:

$$\underline{\underline{\boldsymbol{T}}} = \begin{pmatrix} 1 & s \\ 0 & 1 \end{pmatrix}. \tag{2.16}$$

Another important ray transfer matrix is the refraction matrix $\underline{\underline{\boldsymbol{R}}}$. Using the geometry in figure 2.3 and Snell's Law, $n_1\alpha = n_2\beta$, a linear relation between the input vector $(r_1,\alpha_1)^\top$ and the output vector $(r_2,\alpha_2)^\top$ can be deduced. The resulting shift r_2 after refraction at a curved surface is equal to the initial shift r_1, whereas the input angle α_1 and output angle α_2 differ. Given the geometry in figure 2.3, this yields the relation

$$\alpha - \alpha_1 = -\alpha_2 + \beta = \gamma = \frac{r_1}{R}. \tag{2.17}$$

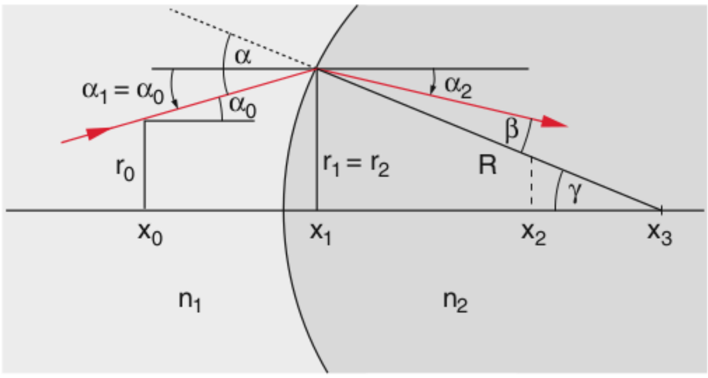

Figure 2.3: The geometry of the refraction of a light ray on a spherically curved surface between two media with respective refractive indices n_1 and n_2. [6]

α_2 is negative due to the convention that the angle is defined as positive when calculated counter clockwise with respect to the positive x-direction.[6] The relationship between α and β according to Snell's Law for small angles, allows the expression above to be modified:

$$n_1\left(\frac{r_1}{R} + \alpha_1\right) = n_2\left(\frac{r_1}{R} + \alpha_2\right). \tag{2.18}$$

Distributing n_1 and n_2 and rearranging terms so as to isolate $n_2\alpha_2$, the refraction on a spherically curved surface can then be expressed with the two equations:

$$\begin{aligned} r_2 &= r_1, \\ n_2\alpha_2 &= n_1\alpha_1 + (n_1 - n_2)\frac{r_1}{R}. \end{aligned} \tag{2.19}$$

The system of equations (2.19) can be expressed as a vector equation:

$$\begin{pmatrix} r_2 \\ n_2\alpha_2 \end{pmatrix} = \begin{pmatrix} 1 & 0 \\ \frac{n_1-n_2}{R} & 1 \end{pmatrix}\begin{pmatrix} r_1 \\ n_1\alpha_1 \end{pmatrix}. \tag{2.20}$$

The matrix which describes a refraction on a spherically curved surface is then dependent on the refractive indices of the two corresponding media as well as the radius of curvature R:

$$\underline{\underline{\boldsymbol{R}}} = \begin{pmatrix} 1 & 0 \\ \frac{n_1-n_2}{R} & 1 \end{pmatrix}. \tag{2.21}$$

Given the derived translation matrix and refraction matrix, it is now possible to derive the matrix describing a lens of arbitrary thickness. A light ray passing through a lens of thickness D consists of a refraction at the first curved surface with radius of curvature R_1, a translation within the lens equal to the distance traveled within the lens d, and a second refraction at the second curved surface with radius of curvature R_2. Figure 2.4 exemplifies the path that a beam may take through a lens. Constructing the necessary matrix to describe a lens $\underline{\underline{\boldsymbol{L}}}$ requires simple matrix multiplication of a refraction matrix $\underline{\underline{\boldsymbol{R}}}_1$, translation matrix $\underline{\underline{\boldsymbol{T}}}_{12}$, and a second refraction matrix $\underline{\underline{\boldsymbol{R}}}_2$:

$$\begin{aligned} \underline{\underline{\boldsymbol{L}}} &= \underline{\underline{\boldsymbol{R}}}_2\, \underline{\underline{\boldsymbol{T}}}_{12}\, \underline{\underline{\boldsymbol{R}}}_1 \\ &= \begin{pmatrix} 1 - \frac{(x_2-x_1)(n_1-n_2)}{n_2R_1} & \frac{x_2-x_1}{n_2} \\ \frac{n_2(n_3-n_2)R_1 - n_2(n_2-n_1)R_2 - (n_3-n_2)(n_2-n_1)(x_2-x_1)}{n_2R_1R_2} & 1 + \frac{(n_3-n_2)(x_2-x_1)}{n_2R_2} \end{pmatrix}. \end{aligned} \tag{2.22}$$

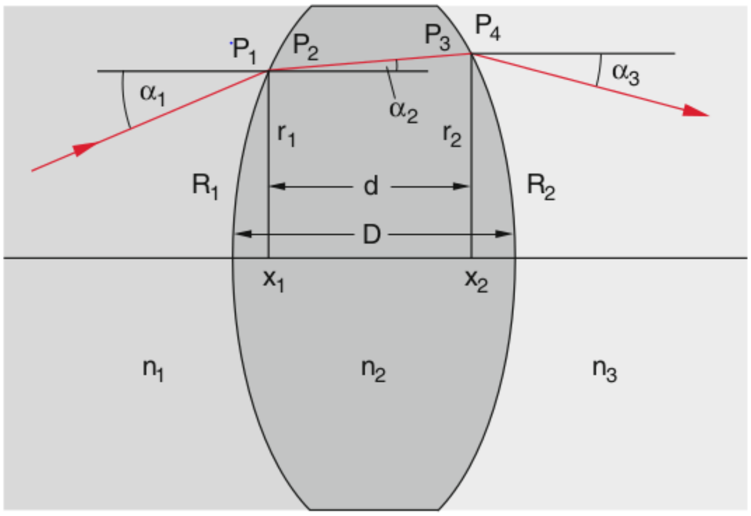

Figure 2.4: Depiction of a lens with thickness D and refractive index n_2. The beam is incident with an angle α_1 on the lens from medium 1 with refractive index n_1, traverses a distance d through the lens with refractive index n_2, and exits with an angle α_3 into medium 3 with refractive index n_3.[6]

In the case of a thin lens in air $n_1 = n_3$ with focal length f and the refractive index $n_2 = n$, the distance $x_2 - x_1$ tends to zero, and the matrix in (2.22) can be immensely simplified to:

$$\underline{\underline{\boldsymbol{L}}}_{\text{thin}} = \begin{pmatrix} 1 & 0 \\ (n-1)\left(\frac{1}{R_2} - \frac{1}{R_1}\right) & 1 \end{pmatrix} = \begin{pmatrix} 1 & 0 \\ -\frac{1}{f} & 1 \end{pmatrix}, \tag{2.23}$$

with the previously derived formula for the focal length (2.11) being used to further simplify the expression.
The matrix derived for the lens with arbitrary thickness typifies the advantage of ray transfer matrices for complex experimental configurations. Through simple matrix multiplication of translation and reflection matrices, a more complex optical component can be described. Moreover, lenses are not the only optical components possible. There are ray transfer matrices for other components such as various types of mirrors, prisms or even matrices for Gaussian beams[23]. This simple matrix multiplication is also not only confined to single optical components, rather entire optical paths through complex systems comprised of many separate optical objects are simplified into single matrices. This allows for simple predictions of the behavior of a light ray in a plethora of experimental situations.

2.3 Operation Amplifiers

Operation Amplifiers, or op-amps, are voltage amplifying devices which were originally designed for performing mathematical operations in analog computations [15]. They are designed to work within circuits consisting of capacitors and resistors and are able to perform a myriad of functions depending on the design of the circuit. In figure 2.5 is a circuit diagramm of an op-amp with differential input and single-ended output as well as supply inputs. [15]

■ Open-Loop Gain

The op-amps differential input consists of the non-inverting (+) input with voltage V_+ and inverting (−) input with voltage V_-. Ideally, only the difference between the voltages V_+ and V_- is amplified, and the output voltage V_{out} is given by the equation:

$$V_{\text{out}} = A_{\text{OL}}(V_+ - V_-), \tag{2.24}$$

with $(V_+ - V_-)$ equal to the voltage V_{diff} and A_{OL} being the gain achieved by the op-amp without a feedback loop from the output to the input (open-loop).

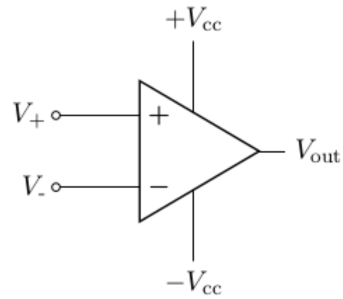

Figure 2.5: Illustration of an operation amplifier in an open-loop form with supply voltage $\pm V_{\text{cc}}$, input voltages V_+ and V_-, as well as the amplified output voltage V_{out}.

Ideal operational amplifiers produce infinite gain and draw zero current from the input source. Futhermore, they exhibit zero resistance to the output load. This means that an ideal op-amp can drive any load without voltage drop occurring due to an output resistance. Moreover, ideal op-amps exhibit an entirely linear relationship between input and output signals. [8, 16, 24]

■ Closed-Loop Gain

Due to physical constraints, ideal characteristics of operational amplifiers are limited to finite quantities. For example, the operational amplifier OP-77 typically achieves a gain of $12 \cdot 10^6$.[8] Predicting and relying on the voltage amplification in an open-loop set-up is, therefore, not realistic, and op-amps are typically built into circuits in a closed-loop form. In this manner, the overall gain and response of the op-amp becomes dependent on the feedback network, for example, additional resistors in the circuit. One such example of a closed-loop circuit, depicted in figure 2.6, is the inverting amplifier. In an inverting amplifier, the output voltage V_{out} changes inversly to the input voltage V_{in}[8]. Using the open-loop gain equation (2.24), an expression for V_{out} with respect to V_{in} can be found. In this case, the resistors behave as a voltage divider, and as a consequence, the voltage at the negative input V_- becomes a function of both V_{in} and V_{out}. V_- may then be expressed as:

$$V_- = \frac{R_{\text{c}} V_{\text{in}} + R_{\text{in}} V_{\text{out}}}{R_{\text{in}} + R_{\text{c}}}. \tag{2.25}$$

When this equation is substituted into equation (2.24), the resulting expression can be solved for the output voltage V_{out} which, in the case that the open-loop gain A_{OL} is large, simplifies to:

$$V_{\text{out}} \approx -\frac{R_{\text{c}}}{R_{\text{in}}} V_{\text{in}}. \tag{2.26}$$

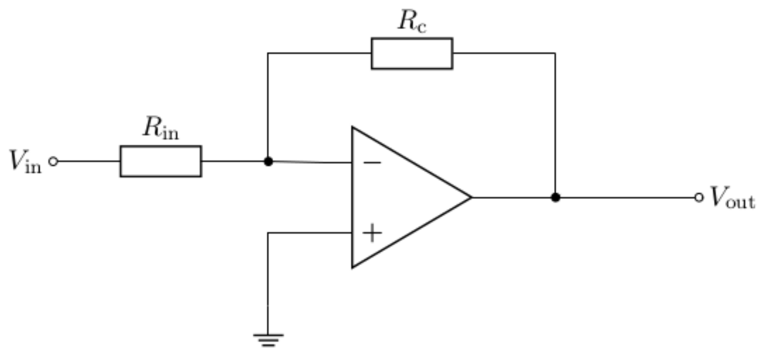

Figure 2.6: Example of an inverting amplifier configuration. The output voltage V_{out} reacts inversely to the behavior of the input voltage V_{in}. The voltage gain that this configuration exhibits is dependent on the ratio of the coupling resistance R_{c} and the initial resistance R_{in}.

■ Transimpedance Amplifierer Circuit

A transimpedance amplifier is used to convert an input electrical current into an output voltage. Often times, the input current is small, for example the currents produced by photodiodes due to electromagnetic radiation, and it is, therefore, advantageous not only to convert the electrical current to a voltage, but also to scale the voltage by use of a resistance R_{c}. In figure 2.7, the input current I_{in} is funneled into the inverting input of the op-amp and converted to an output voltage V_{out}. Accordingly the output voltage V_{out} is given by the expression[24]:

$$V_{\text{out}} = -R_{\text{c}} I_{\text{in}}, \tag{2.27}$$

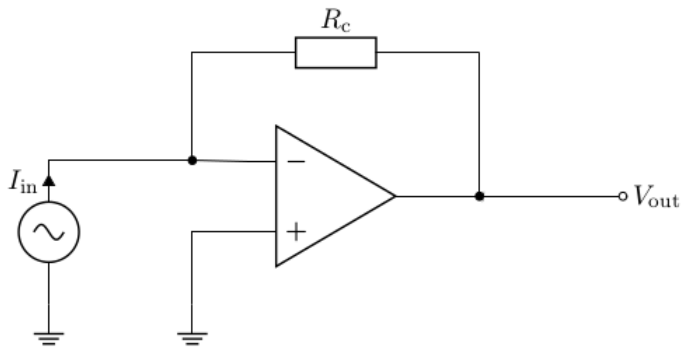

Figure 2.7: An illustration of an op-amp configuration utilized to convert an electrical input current I_{in} into a corresponding output voltage V_{out} which is scaled by a factor equal to the coupling resistance R_{c}.

2.4 Transistors as Switches

A transistor is a device composed of semiconducting materials which is used to amplify or switch electronic signals.[13] The functionality of transistors is based on np-junctions.

For example, in the case of a bipolar junction transistor, two np-junctions are placed together to form either a npn-transistor or pnp-transistor. Deploying transistors such as bipolar junction transistors in circuits at one point can enable control over the flow of current at another position in the circuit. A bipolar junction transistor has three terminals labeled base, collector, and emitter. In figure 2.8 a circuit using a npn-bipolar transistor to realize an electrical switch is shown. If zero voltage is applied between the base and emitter, almost no current flows from the collector to the emitter. If, however, the voltage at the base begins to increase, then the current between collector and emitter increases exponentially, and a voltage drop occurs due to the reduction in resistance. If current flows between collector and emitter, the transistor is said to be saturated, whereas if no current flows, the transisor is in the so-called cutoff mode.[12]

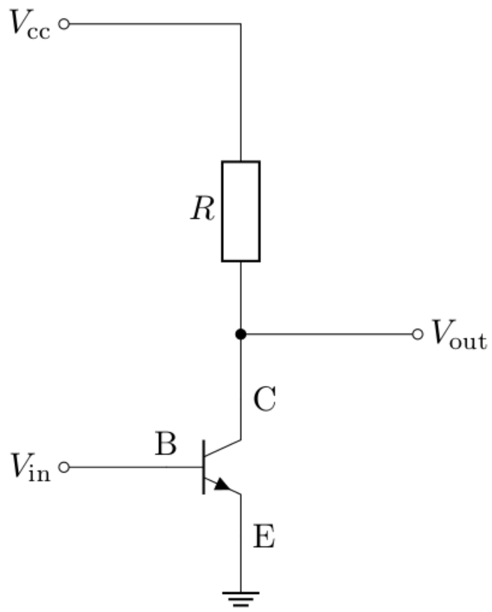

Figure 2.8: Depiction of a npn-bipolar junction transistor with the three terminals, base B, Emitter E, and collector C, in a circuit. The current between emitter and collector depends on the input voltage at the base V_{in} as well as the voltage V_{cc} and the chosen resistor R. The emitter is fed to ground whereas the output voltage V_{out} lies between the collector and the supply voltage V_{cc}.

2.5 Photodiodes

A photodiode is a semiconductor device which converts electromagnetic waves into electrical current by the exploitation of the inner photoelectric effect. If photons with an energy greater than the electronic band gap of the semiconducting material are absorbed by electrons in the valence band, then the electrons will excite into the conduction band leaving behind a hole which acts as a positive charge carrier. If the absorption of a photon occurs in the depletion region of the junction, then the electron and hole are forced to flow to the cathode and anode respectively. This charge flow manifests itself as a photocurrent, which is proportional to the power of the light source. The ratio of photocurrent produced in response to the power of a light source is known as the photosensistivity S. Placing four photodiodes together in a quadrant configuration enables not only the sensing of photons but also spatial recognition of where the light strikes the photosensitive area spanned by the four photodiodes. The photocurrent produced by one diode may differ from the photocurrent produced by another depending on the position of light on the surface. This becomes useful, for example, when the precise knowledge of the position of a laser beam is important or necessary.[11]

Chapter 3

Imaging Scheme

The imaging scheme developed for Rydberg experiments, as described in chapter 1, features an in-vacuum mirror which exhibits unpredictable tilt. In order to correct for this variability in tilt the imaging set-up is predicated on a telescopic configuration of two bi-convex lenses and a motorized gimble mount for a dielectric mirror. A laser beam passing through the set-up will strike the problematic mirror at a point in the center, irregardless of the angle of incidence of the beam. This is possible due to the fact that the angular deflection spurred by the gimble mirror is imaged onto the in-vacuum mirror. The configuration of the lenses can be justified both theoretically and experimentally. The motorized gimble mount enables the variability of the angle of incidence on the tilted mirror which, in turn, modifies the angle of reflection of the beam. Accordingly, varying degrees of tilt can be accounted for and are able to be corrected. Automation of the angle adjustments is then programmed with the use of a micro controller. The voltages used to operate the motorized actuators of the gimble mount are coordinated with the recognition of voltages received from a quad segment photodiode placed at the back of the imaging scheme. The entire imaging apparatus is, therefore, divided into three separate segments: the optical set-up which realizes the correction of the tilted mirror, the electronic set-up which enables the automation of the correction, and the automation itself which is realized by means of a micro controller and the correction algorithm.

3.1 Optical Set-Up

■ Mathematical Justification for the Optical Set-Up

The optical set-up depends entirely on the ability to alter the angle of incidence of a laser beam striking the tilted mirror, while simultaneously preventing the displacement of the beam. This problem can treated mathematically by means of ray transfer analysis already presented in the previous chapter 2. In this case, the input vector will have the initial components $r_1 = 0$ and $\alpha_1 = \alpha$. This implies that the beam begins its path on the optical axis with an arbitrary angle made with the axis of α. The laser then performs a translation of distance d_1 before striking a thin convex lens with the focal point f_1. After leaving the first lens and traveling a distance d_2, the beam passes a second thin convex lens with focal length f_2. Finally, the beam meets with the tilted mirror at a distance d_3, and the output vector is given by the components $r_2 = r_1 = 0$ and $\alpha_2 = \alpha'$. An illustration of the problem is given in figure 3.1. Quantitatively, this problem is described by the multliplication of the input vector $\boldsymbol{\nu}_1$ from right to left with two thin lens matrices $\underline{\underline{\boldsymbol{L}_1}}$ and $\underline{\underline{\boldsymbol{L}_2}}$ and three translation matrices $\underline{\underline{\boldsymbol{T}_1}}$, $\underline{\underline{\boldsymbol{T}_2}}$, and $\underline{\underline{\boldsymbol{T}_3}}$ which yields the desired output vector $\boldsymbol{\nu}_2$:

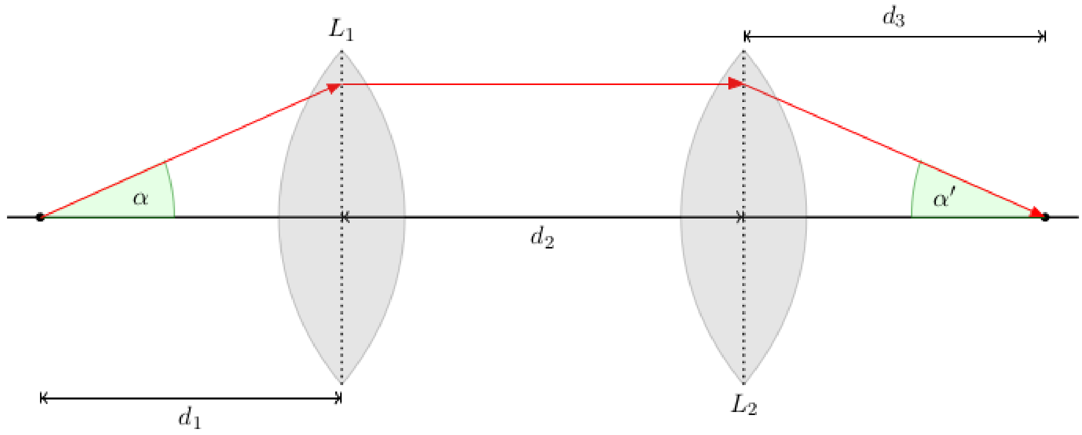

Figure 3.1: Depiction of the two lens optical configuration. The laser beam performs a translation of distance d_1 before passing the first lens L_1. A second translation of distance d_2 occurs between the two lenses L_1 and L_2. Finally, the beam strikes the mirror after a translation of d_3.

$$
\begin{aligned}
&\boldsymbol{\nu}_2 = \underline{\underline{\boldsymbol{T}_3}} \cdot \underline{\underline{\boldsymbol{L}_2}} \cdot \underline{\underline{\boldsymbol{T}_2}} \cdot \underline{\underline{\boldsymbol{L}_1}} \cdot \underline{\underline{\boldsymbol{T}_1}} \cdot \boldsymbol{\nu}_1 \\
\implies &\begin{bmatrix} 0 \\ \alpha' \end{bmatrix} = \begin{bmatrix} 1 & d_3 \\ 0 & 1 \end{bmatrix} \cdot \begin{bmatrix} 1 & 0 \\ -\frac{1}{f_2} & 1 \end{bmatrix} \cdot \begin{bmatrix} 1 & d_2 \\ 0 & 1 \end{bmatrix} \cdot \begin{bmatrix} 1 & 0 \\ -\frac{1}{f_1} & 1 \end{bmatrix} \cdot \begin{bmatrix} 1 & d_1 \\ 0 & 1 \end{bmatrix} \cdot \begin{bmatrix} 0 \\ \alpha \end{bmatrix} \\
&= \begin{bmatrix} 1 - d_3\left(\frac{1}{f_1} + \frac{1}{f_2}\right) - \frac{d_2}{f_1}\left(1 - \frac{d_3}{f_2}\right) & d_3 + d_2\left(1 - \frac{d_3}{f_2}\right) + d_1\left(1 - \frac{d_3 + d_2\left(1 - \frac{d_3}{f_2}\right)}{f_1} - \frac{d_3}{f_2}\right) \\ -\frac{1 - \frac{d_2}{f_2}}{f_1} - \frac{1}{f_2} & 1 - d_1\left(\frac{1 - \frac{d_2}{f_2}}{f_1} - \frac{1}{f_2}\right) - \frac{d_2}{f_2} \end{bmatrix} \cdot \begin{bmatrix} 0 \\ \alpha \end{bmatrix}.
\end{aligned} \tag{3.1}
$$

The resulting equation (3.1) can be rewritten as the system of equations:

$$
\begin{aligned}
0 &= \left[d_3 + d_2\left(1 - \frac{d_3}{f_2}\right) + d_1\left(1 - \frac{d_3 + d_2\left(1 - \frac{d_3}{f_2}\right)}{f_1} - \frac{d_3}{f_2}\right)\right]\alpha, \\
\alpha' &= \left[1 - d_1\left(\frac{1 - \frac{d_2}{f_2}}{f_1} - \frac{1}{f_2}\right) - \frac{d_2}{f_2}\right]\alpha.
\end{aligned} \tag{3.2}
$$

There exists a non-trivial solution to this system of equations (3.2) when the translation distances d_1, d_2, and d_3 are chosen to be dependent on the focal lengths of the two lenses f_1 and f_2. If $d_1 = f_1$, $d_2 = f_1 + f_2$, and $d_3 = f_2$, then the first equation becomes fulfilled, and the expression for the angle α' is equal to:

$$
\alpha' = -\frac{f_1}{f_2}\alpha. \tag{3.3}
$$

Equation (3.3) means a linear relationship between α' and α with a slope dependent on the chosen focal lengths f_1 and f_2.

Although the only non-trivial solution to the system of equations in (3.2) requires the precise placement of the lenses with respect to the optical path, the question arises, to what extent the optical set-up remains robust in the presence of deviations. Considering once again the vector equation (3.1) and substituting the distances determined above as well as introducing arbitrary error distances $d_1 = f_1 + \delta$, $d_2 = f_1 + f_2 + \chi$, and $d_3 = f_2 + \epsilon$, the equation becomes:

$$\begin{bmatrix} 0 \\ \alpha' \end{bmatrix} = \begin{bmatrix} 1 & f_2 + \epsilon \\ 0 & 1 \end{bmatrix} \cdot \begin{bmatrix} 1 & 0 \\ -\frac{1}{f_2} & 1 \end{bmatrix} \cdot \begin{bmatrix} 1 & f_1 + f_2 + \chi \\ 0 & 1 \end{bmatrix} \cdot \begin{bmatrix} 1 & 0 \\ -\frac{1}{f_1} & 1 \end{bmatrix} \cdot \begin{bmatrix} 1 & f_1 + \delta \\ 0 & 1 \end{bmatrix} \cdot \begin{bmatrix} 0 \\ \alpha \end{bmatrix}. \tag{3.4}$$

The error distances δ, χ, and ϵ represent a suboptimal realization of the distances between the optical components necessary to fulfil the expression in equation (3.3). δ corresponds to a shift of the first lens from the correcting mirror, and ϵ represents a shift of the second lens relative to the tilted mirror. χ is the shift in distance between the two lenses which consists of the shifts δ and ϵ. Solving the vector equation above (3.4) leads to three solutions. The two trivial solutions are either when both the input angle α and the output angle α' are equal to zero, or α' is equal to the above expression (3.3) when the error distances tend to zero. The only non-trivial solution to the vector equation is given by:

$$\alpha' = \frac{f_2 \delta}{f_1 \epsilon} \alpha, \text{ when } \chi \to \frac{f_1^2 \epsilon + f_2^2 \delta}{\epsilon \delta}. \tag{3.5}$$

Because it would be disadvantageous to adjust the distance between the two lenses as opposed to changing the distance of one lens with respect to the other, the condition for χ in equation (3.5) should be solved for ϵ and δ. Dividing both sides of the conditon for χ by f_1^2 and assuming that the square of both of the focal lengths is much greater than the individual error distances δ, χ, and ϵ, leads to the expression:

$$\begin{aligned} \frac{\chi}{f_1^2} &= \frac{1}{\delta} + \frac{f_2^2}{f_1^2 \epsilon} \approx 0 \\ \implies \delta &\approx -\frac{f_1^2}{f_2^2} \epsilon. \end{aligned} \tag{3.6}$$

Plugging δ from (3.6) into the expression for α' in (3.5) yields the same equation (3.3) as if the optical components were optimally installed. This implies that an adjustment of the one of the two lenses can sufficiently correct for a suboptimal installment of the optical components. In this particular optical set-up $f_1 = 250\,\text{mm}$ and $f_2 = 250\,\text{mm}$ which leads to $\alpha' = -\alpha$.

■ Experimental Justification for the Optical Set-Up

During the implementation of the optical components necessary to realize the optical set-up, it was discovered that the configuration did not operate as intended. Matrix analysis of the beam path suggests that the beam will remain stable at the center of the tilted mirror even when the angle of the beam made with the axis is altered. This was, however, not observed, rather, the beam appeared to significantly wander from the center of the tilted mirror when the initial angle α produced by the motorized mirror was varied. In order to more precisely quantify these deviations, a CCD camera was placed at the position where the tilted mirror would be located, and the position of the laser beam on the camera was recorded for various initial angles δ_x and δ_y produced by the motorized mirror. These angles correspond to the possible orientations of the mirror relative to the original position, 45° to the optical axis. The positions of the beam on the camera were then calculated by fitting a Gaussian beam profile to the images. The distances away from the center of the mirror were then plotted in a heat map for various motor mirror orientations which is displayed in figure 3.2a. As is seen in figure 3.2a, the angles of tilt of the motor mirror ranged from 0° to 2.3°, and the extent of deviation Δ of the beam from the center of the tilted mirror ranged from $\Delta = 0\,\mu m$ to $\Delta \approx 1300\,\mu m$.

The deviations were later determined to be due to the mount which housed the correcting mirror. The mirror mount performed not only a tilt of the mirror in the xy-plane but also caused a shift $r_1 = r_2 \neq 0$ of the beam along its path. This additional translation of the beam exhibited a dependence on the tilt angles δ_x and δ_y and caused an unacceptable movement of the beam. The solution was to install a gimble mount to house the correcting mirror. The gimble mount does not cause an additional translation while rotating, and as a consequence, the beam strayed to a significantly lesser degree from the center of the tilted mirror. Analagously, to the measurements performed to determine the deviation of the beam for various correcting mirror orientations in the case of the mirror mount, a heatmap was constructed in the case of the gimble mount. Using the same scaling as in figure 3.2a, The beam exhibits considerably less deviation, and peak deviation in the case that $\delta_x = 2.3°$ and $\delta_y = 2.3°$ was less than half of a millimeter. This can be seen in figure 3.2b

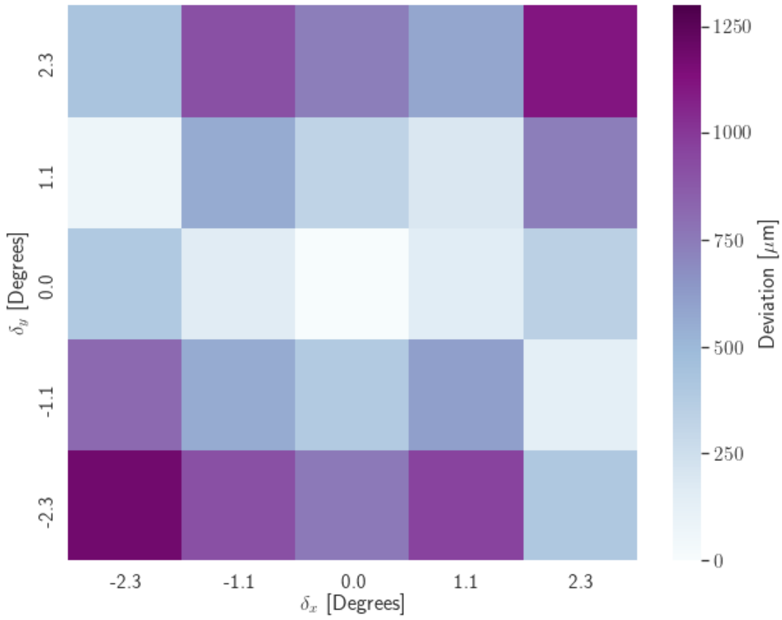

(a) The range of deviation of the beam when using the mirror mount.

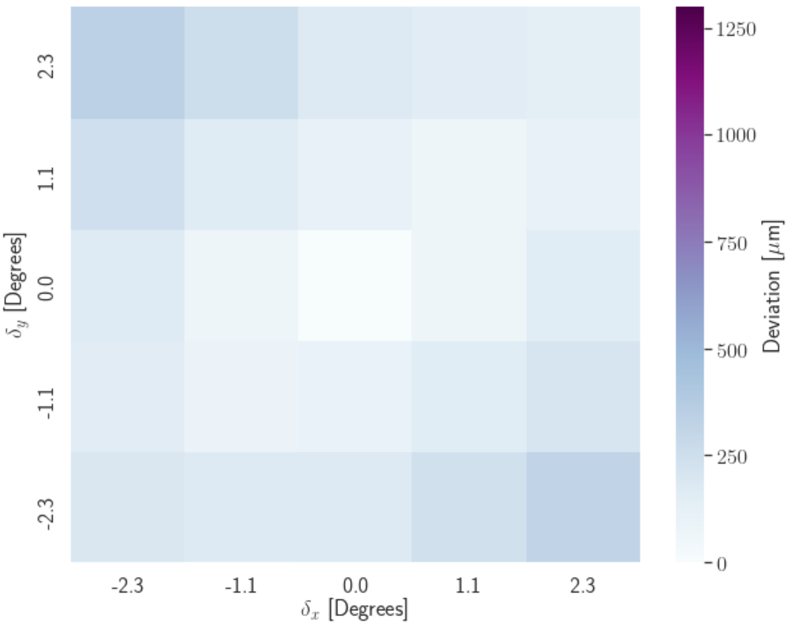

(b) The range of deviation of the beam when using the gimble mirror mount.

Figure 3.2: Determination of the extent of displacement of the beam from the optical axis at the center of the tilted mirror relative to varying initial angles δ_x and δ_y produced by the motorized mirror. For the measurements, two separate types of mounts were used with the motor actuators to house the one inch dielectric mirror.

■ Realisation of the Optical Set-Up

Figure 3.3 represents the entirety of the optical set-up. Lenses L_1 and L_2 are 2 inch, achromatic, biconvex lenses with focal lengths $f_1 = 250\,\mathrm{mm}$ and $f_2 = 250\,\mathrm{mm}$[1]. L_1 is mounted with the relatively less curved side directed toward the self-adjusting mirror (SAM), and the less curved surface of L_2 points in the direction of the tilted mirror (TM). This, in conjunction with the doublet design of the lenses, minimizes spherical aberrations. The distance between the lenses is equal to the sum of both focal lengths $d_2 = f_1 + f_2 = 500\,\mathrm{mm}$, and the distance between SAM and the first lens, as well as the second lens to TM is equal to the respective focal lengths of each of the lenses $d_1 = f_1 = d_3 = f_2 = 250\,\mathrm{mm}$. The distances were chosen based on the spatial contraints dictated by the experimental set-up. L_2 is 16 mm away from the edge of the metal platform, represented by the shaded region in figure 3.3. The total beam path to the tilted mirror is 1000 mm. In order to achieve this length, given the dimensions of the platform, three 2 inch fixed dielectric mirrors[2] are implemented. The 0.8 mW 633 nm helium-neon laser beam passes through the test set-up at a height 44 mm above the metal platform, and in the actual absorption imaging experiments, this laser will be replaced by a 780 nm-laser and a 671 nm-laser.

The self-adjusting mirror is composed of a gimble mount used to house a 1 inch dielectric mirror[3] which is suited with two motorized actuators[4] connected to two DC servo motor controllers[5]. The travel range of the actuators is 12 mm, and electromechanical limit switches prevent over rotation of the screw in both directions. The servo motor drivers are designed to operate with up to 15 V/2.5 W motors, and the characteristics of the servo drivers in addition to the motor actuators can be set through the use of the APT software provided by Thorlabs. The APT software enables control over the velocity profile settings, limit switch handling, a homing functionality, as well as spontaneous changes to speed and direction. The jogging function of the drivers allows for either continuous or step functionality, and the smallest reliable step size for the actuators, provided by the drivers, is 5 µm. Furthermore, the motor controllers have been modified with an external circuit separated from the internals by an opto-isolator, which operates the jog function in both directions using an LVTTL-signal. Through the APT software, so-called parameter sets can be saved, which are then installed on the servo motor drivers temporarily until the motors are turned off. There is a persist to hardware setting which would theoretically allow the parameter sets to be saved locally on the servo motors indefinitely; however, while attempting to take advantage of this functionality, it did not operate as intended. As a consequence, it is necessary to reinstall the parameter set each time the motors are seperated from the supply voltage.

After the laser strikes the ½ inch tilted mirror[6], it traverses through an aperature in the form of a pinhole (PH), 743 mm away with a diameter of 4 mm. The beam then passes a ½ inch biconvex lens L_3 with focal length $f_3 = 26\,\mathrm{mm}$ which represents an in-vacuum aspheric lens providing high numerical aperture optical access to the atomic cloud. It converges at the focal point F_3 and then begins to diverge before being reflected 90° by the fixed mirror FM4. Because the divergence of the beam is too large for the $10\,\mathrm{mm}^2$ surface area of the quad segment diode (QD) to spatially resolve, the beam waist must be reduced. This additional convergence of the laser is realized by means of an additional lens

[1] Thorlabs AC254-250-B
[2] Thorlabs BB2-E02
[3] Thorlabs BB2-EO2
[4] Thorlabs Z812 motorized DC servo actuators
[5] Thorlabs TDC001 T-cube DC servo motor controllers
[6] Thorlabs BB1-E02

configuration of two 2 inch, biconvex lenses L_4 and L_5, each with focal lengths $f_4 = 250\,\mathrm{mm}$ and $f_5 = 100\,\mathrm{mm}$ respectively. The photodiode is placed slightly behind the focal point F_5 at a distance 110 mm away from L_5. At this distance, the beam waist is small enough so as to produce differing photocurrents relative to the position on the surface of the quad diode, while still enabling the beam to stray due to varying angles of incidence produced by the correcting mirror.

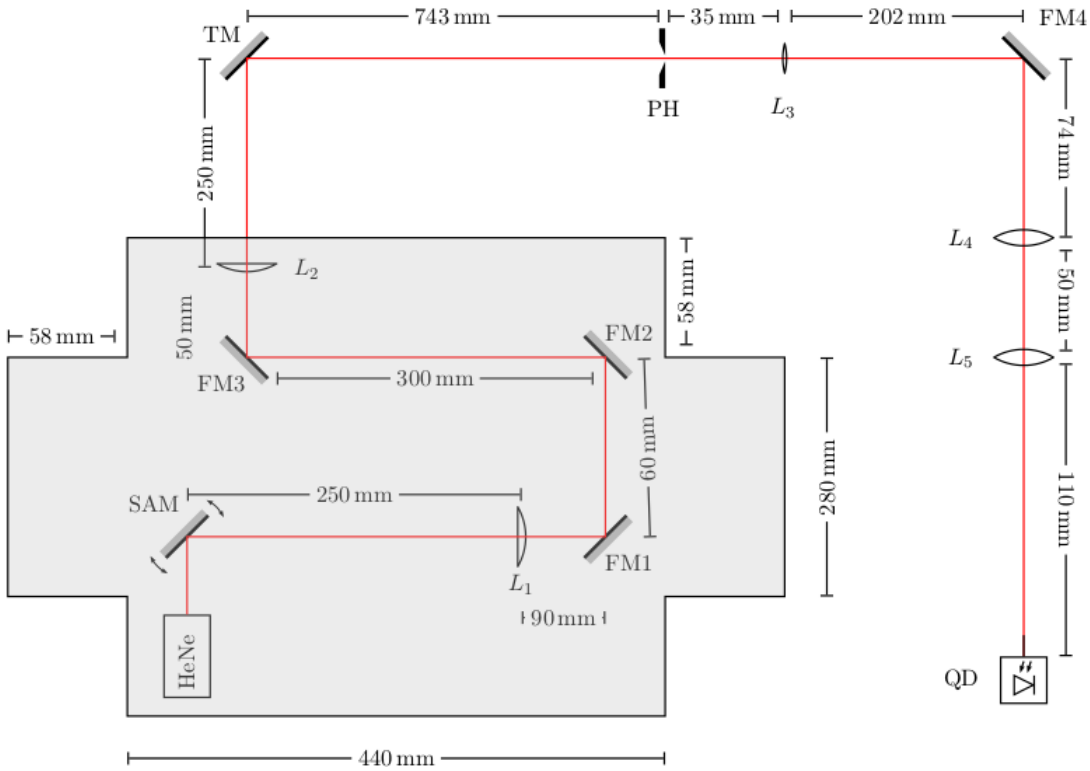

Figure 3.3: Depiction of the optical set-up deployed to correct for the tilted mirror TM inside the ion microscope. The shaded surface is the scheme which corrects for the tilt based on the photocurrents recieved from the quad segment photodiode (QD). The correction occurs based on changes in the angle of incidence of the 632 nm-HeNe-laser beam by use of the self-adjusting mirror (SAM). Due to the focal lengths of the lenses L_1 and L_2, the total distance the beam must travel before striking TM is 1000 mm, and this is accomplished by use of fixed dielectric mirrors (FMX). Lenses L_3, L_4, and L_5, as well as the pin-hole aperature (PH) are a part of the imaging scheme which mimics the conditions inside and outside the ion microscope.

3.2 Electronic Set-Up

The electronic set-up used to automate the adjustment process of the correcting mirror is realized by means of a Teensy 3.2 micro controller. The servo motor controllers used to drive the motorized actuators for the gimble mount can be controlled via LVTTL-signals supplied by the micro controller. Moreover, the micro controller has the ability to read the voltages produced by the three outputs of the the quad segment diode installed to sense the position of the laser beam. One of the outputs corresponds to the total voltage V_{tot} produced by the photodiode in response to light, and the other two outputs V_{12} and V_{13} are responsible for the spatial resolvability of the beam. The latter two outputs pose a problem, as the possible voltages can be negative. As a result, the circuitry for the segment diode had to be modified. This was achieved by use of an additional circuit which provides a variable attenuation of the output voltages as well as a direct voltage offset. The coordination of the driving of the actuators in response to the information garnered from the photodiode was realized with a programm written in the Arduino language loaded on the micro controller.

■ Teensy 3.2 Micro Controller

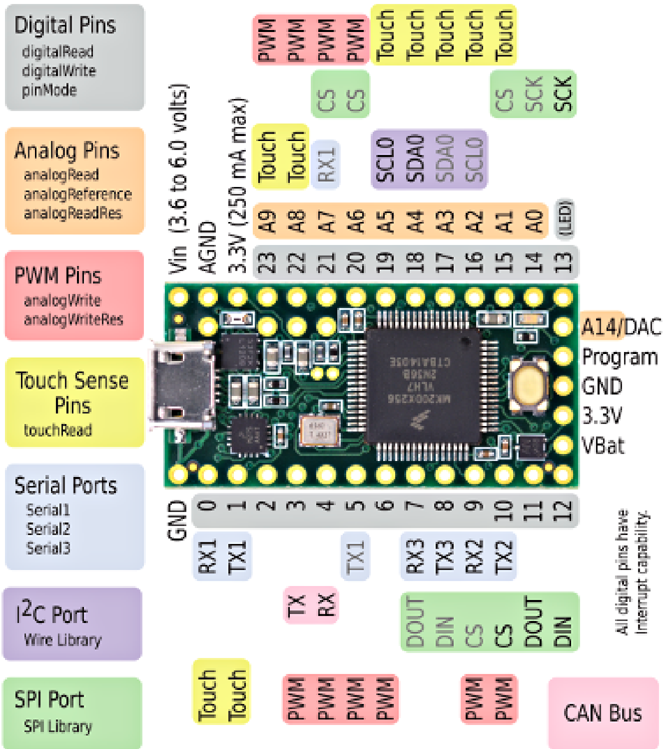

Figure 3.4: Illustration of the Teensy 3.2 micro controller pinout used to coordinate the driving of the motor actuators with the information registered from the quad segment diode. [21]

The Teensy 3.2 micro controller shown in figure 3.4 is suited with 34 digital I/O pins with a maximum voltage output of 3.3 V and a voltage input tolerant up to 5 V. The 21 available analog pins are also able to output 3.3 V; however, the input voltage tolerance is only 3.3 V. The analog input resolution is 16 bits. [21]

Figure 3.5 is a representation of the configuration and chosen pins for the motor drivers and the photodiode connections. The resistance R_{cc} is the resistance used for all four transistor switches for the pins D14, D17, D20, and D23. The voltage regulator[7] maintains a stable 5 V power supply for the micro controller. Stability for the voltage regulator is provided by the capacitors C_{cc} = 224 nF and C_g = 100 nF. For the total voltage connection of the photodiode, a voltage divider with variable resistace is necessary in order to restrict voltage to the range between 0 V and 3.3 V. The output of the voltage divider is connected to the analog pin A8. The two other output voltages V_{12} and V_{13} of the photodiode are connected to the pins A7 and A5 respectively.

[7] LM7805

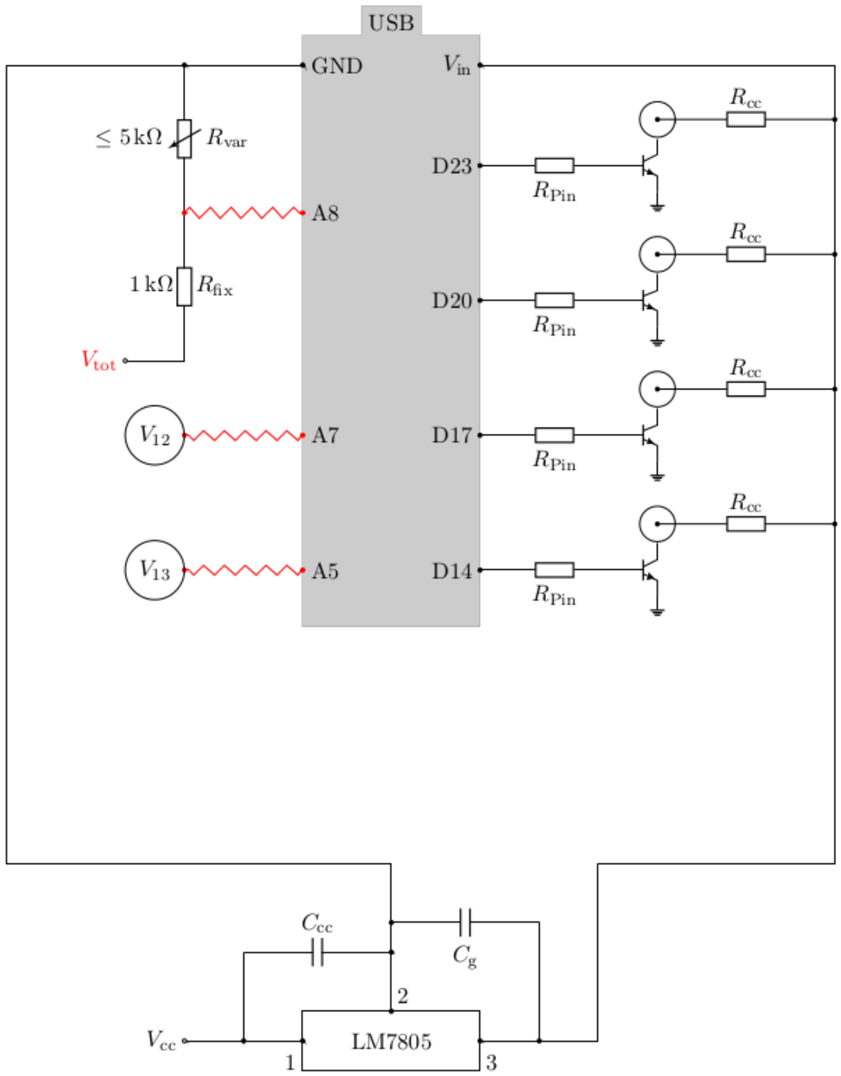

Figure 3.5: Complete configuration of the micro controller with the digital pins D23, D20, D17, and D14 used for the two servo motor drivers, as well as the implemented transistor switches. The photodiode connections are marked in red and are connected to the analog pins A5, A7, and A8. The capacitors are there to stabilize the 5 V voltage regulator *LM7805* implemented to supply the voltage powering the Teensy 3.2. The pins of the voltage regulator are numbered: 1 corresppvonds to the input voltage, 2 corresponds to ground and three corresponds to the output of the voltage regulator.

■ Connecting the Motors

The servo motor controllers driving the motorized actuators are each suited with two external female BNC connections used to drive the actuators with an external LVTTL-signal connected to the jog function, forward and reverse. The internal circuitry of the servo motors is separated from the external BNC connections by an opto-isolator which requires a current to operate that the pins of the micro controller are unable to provide. As a result, transistor switches were implemented at each of the four pins of the micro controller. Figure 3.6 illustrates the transistor switch used to provide sufficient voltage to the motors. The transistor remains in the cutoff mode as long as there is no voltage produced by the pin.

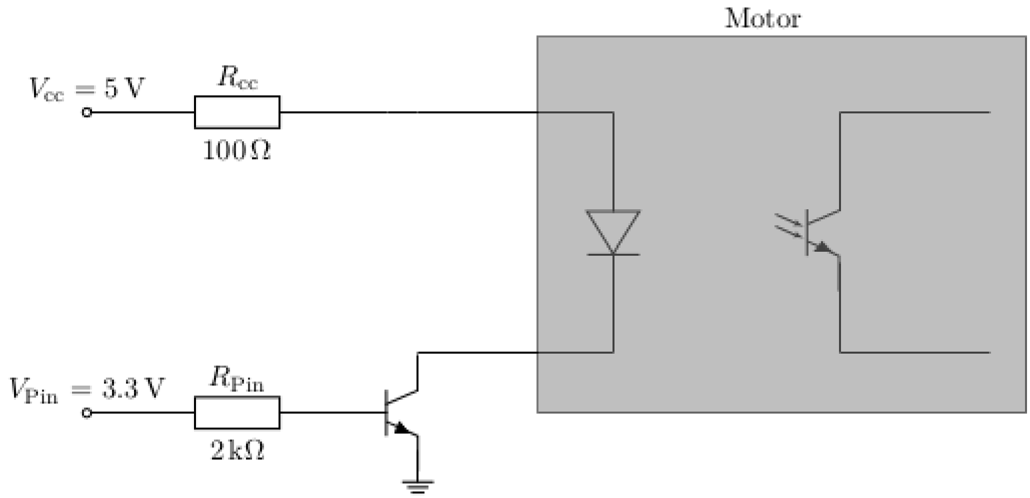

Figure 3.6: The transistor switches implemented in order to control the servo motors. When the voltage at $V_{Pin} = 3.3\,V$ the npn-bipolar junction transistor saturates, and a collector emmiter current is produced which switches the opto-isolator. The shaded region represents the servo motor with the opto-isolator.

■ Connecting the Quad Diode

A quad segment photodiode is used to sense the position of the beam at the end of the imaging scheme[8]. The photosensitive area consists of four elements with a total surface area of $10\,mm^2$. The spectral response range is between 320 nm and 1100 nm with a peak sensitivity of 0.72 A/W at 960 nm. The total spectral response curve with photosensistivity plotted over the wavelength is given in the datasheet for the photodiode.[26]

In order to convert any photocurrents generated by the quad diode to measurable voltages, each element of the four segments is connected to a transimpedance amplifier shown in figure 3.9. The respective output voltages are given by $V_i = -R_i I_{photo}$, where I_{photo} is the photocurrent and $R_i = 10\,k\Omega$. After the voltages are produced, the outputs V_i are funneled into three separate circuits. The first circuit, depicted in figure 3.8, sums over the voltages V_1, V_2, V_3, and V_4 resulting in an output voltage corresponding to the total voltage generated by the four segments. The second circuit adds the voltages V_1 and V_3 together while subtracting the voltages V_3 and V_4 resulting in the output voltage v_{12}. The third circuit functions analagously to the second one with the voltages V_1 and V_3 being summed together and the voltages V_2 and V_4 being subtracted away, leading to the output voltage v_{13}. The two circuits with output voltages v_{12} and v_{13} are shown in figure 3.10.

Because the pins of the micro controller are only able to withstand positive input voltages up to 3.3 V, a voltage divider using a variable resistance was placed before the analog pin for the circuit in figure 3.8. This enables the possibility of attenuating any photovoltages produced by the photodiode in response to various laser powers. For example, the spectral response of the photodiode from a laser with a wavelength $\lambda = 800\,nm$[9] is approximately 0.6 A/W. Now, if an imaging intensity corresponding to 8 % of the saturation intensity $I_{sat} = 1.669\,mW/cm^3$ is assumed for the hyperfine levels of ^{87}Rb

[8] S5980 Si PIN photodiode from HAMAMATSU

[9] This wavelength is easily obtained from the datasheet and is reasonably close to the relevant 780 nm

$|F=2, M_F=\pm 2\rangle \rightarrow |F'=3, M_{F'}=\pm 3\rangle$ relevant for the absorption imaging being performed with the ion microscope [1], the photocurrent and subsequent voltage from the segment diode can be determined. For the approximation, the diameter of the beam is assumed to be $d_s = 1.5\,\text{mm}$:

$$\begin{aligned} P &= 0.08(P_{\text{tot}}) = 0.08\left(I_{\text{sat}} d_s^2\right) = 0.08\left(I_{\text{sat}} 4 r_s^2\right) \\ \Longrightarrow P &= 0.08\left[1.669\,\text{mW/cm}^2 \cdot (1.5\,\text{mm})^2\right] \\ &= 3.00\,\text{mW}. \end{aligned} \tag{3.7}$$

The photocurrent I_{photo} then becomes the product of the power obtained above in (3.7) with the spectral response S:

$$\begin{aligned} I_{\text{photo}} &= SP \\ \Longrightarrow I_{\text{photo}} &= 0.6\,\frac{\text{A}}{\text{W}} \cdot 3.00\,\text{mW} \\ &= 1.80\,\text{mA}. \end{aligned} \tag{3.8}$$

The photocurrent is then converted to a voltage V_{photo}:

$$\begin{aligned} V_{\text{photo}} &= 1.80\,\text{mA} \cdot 10\,\text{k}\Omega. \\ &= 18\,\text{V} \end{aligned}$$

This voltage must, therefore, be attenuated by a factor of approximately five for the voltage to be compatible with the input pin of the micro controller. This is accomplished with the voltage divider in figure 3.5. The attenuation of the photovoltage V_{dv} depends on the variable resistor R_{var} and the resistor $R_{\text{fix}} = 1\,\text{k}\Omega$[10]:

$$V_{\text{dv}} = \frac{R_{\text{fix}}}{R_{\text{var}} + R_{\text{fix}}} V_{\text{photo}} \tag{3.9}$$

$$\Longrightarrow \frac{3.3\,\text{V}}{18\,\text{V}} = \frac{R_{\text{fix}}}{R_{\text{var}} + R_{\text{fix}}} \tag{3.10}$$

$$0.18 \approx \frac{1\,\text{k}\Omega}{R_{\text{var}} + 1\,\text{k}\Omega}. \tag{3.11}$$

This leads to the variable resistor needing to be set to a resistance of $4.45\,\text{k}\Omega$.

The Teensy 3.2 is only able to read voltages between 0 V and 3.3 V. This means that the voltage range $\pm 15\,\text{V}$ possible from the outputs v_{12} and v_{13} in figure 3.10 must be modified in order to be compatible with the pins of the micro controller[11]. This can be achieved by inserting an additional circuit after the two initial transimpedance amplifiers of the two outputs v_{12} and v_{13}. The total voltage range of the op-amps can be mapped onto the compatible voltage range appropriate for the micro controller and the additional circuit is represented by the shaded region in figure 3.7. The circuit provides a non-inverting attenuation of the possible voltage range of the output voltages v_{12} and v_{13}, as well as a positive voltage offset. This corresponds to an output voltage function in the form of a straight line with a positive slope and a positive y-intercept. The slope m of the output voltage function is equal to the ratio of the voltage range possible for the micro controller

[10] 1833.2081 5 kΩ MENTOR

[11] It is important to note that the circuit was already given. Otherwise, a considerably more practicle circuit would have been contstructed which would circumvent this problem and yield the necessary voltage outputs

$V_{\text{out,+}} - V_{\text{out,-}}$ to the voltage range possible for v_{12} and v_{13}:

$$\begin{aligned} m &= \frac{V_{\text{out,+}} - V_{\text{out,-}}}{V_{\text{in,+}} - V_{\text{in,-}}} \\ \implies m &= \frac{3.3\,\text{V} - 0\,\text{V}}{15\,\text{V} - (-15\,\text{V})} \\ &= 0.11, \end{aligned} \tag{3.12}$$

with $V_{\text{in,+}} - V_{\text{in,-}}$ corresponding to the voltage range of the outputs v_{12} and v_{13}.

The y-intercept b is then given by the equation:

$$\begin{aligned} b &= V_{\text{out,-}} - mV_{\text{in,-}} \\ \implies b &= 0\,\text{V} - 0.11 \cdot (-15\,\text{V}) \\ &= 1.65\,\text{V}. \end{aligned} \tag{3.13}$$

The slope m corresponds to the gain of the circuit. Considering the configuration in figure 3.7, m can be rewritten dependent on the resistors R_{in}, R_{ref}, and R_{g}:

$$m = \frac{\frac{1}{R_{\text{in}}}}{\frac{1}{R_{\text{in}}} + \frac{1}{R_{\text{g}}} + \frac{1}{R_{\text{ref}}}}. \tag{3.14}$$

Similarly, the y-intercept can be rewritten with respect to the reference voltage V_{ref} and the resistors R_i:

$$b = V_{\text{ref}} \frac{\frac{1}{R_{\text{ref}}}}{\frac{1}{R_{\text{in}}} + \frac{1}{R_{\text{g}}} + \frac{1}{R_{\text{ref}}}}. \tag{3.15}$$

In order to achieve the necessary gain and DC-offset from the equations above, the reference voltage V_{ref} is equal to 5 V. This was realized by use of a 5 V voltage regulator[12] to attenuate the +15 V powering the op-amps. The resistors available for the circuit differed slightly from the theoretical values $R^0_{\text{in}} = 620\,\Omega$, $R^0_{\text{ref}} = 200\,\Omega$, and $R^0_{\text{g}} = 120\,\Omega$. The actually implemented resistances were equal to $R_{\text{in}} = 680\,\Omega$, $R_{\text{ref}} = 196\,\Omega$, and $R_{\text{g}} = 120\,\Omega$. Subsequently, the gain m and the DC-offset vary tolerably from the expectation.

[12] LM8705

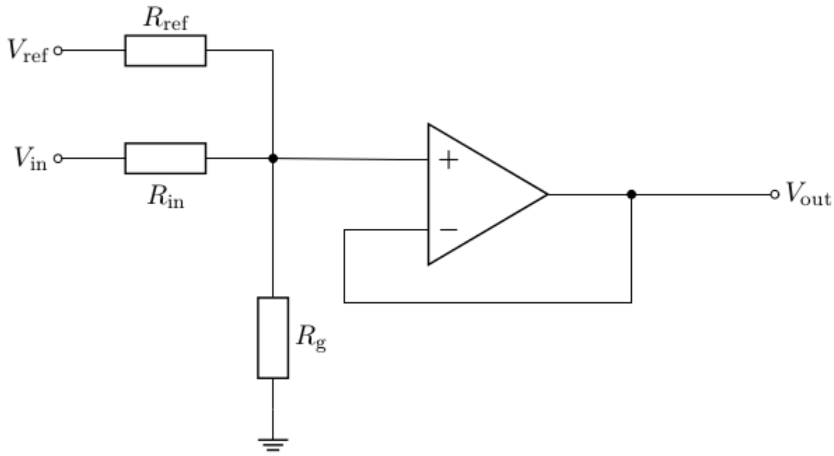

Figure 3.7: The additional circuit to provide a linear voltage output in the form of a straight line with slope m and y-intercept b. The reference voltage V_{ref} is utilized to provide a DC-offset. The slope corresponds to the gain which is dependent on the combination of resistances R_i. (see body of text)

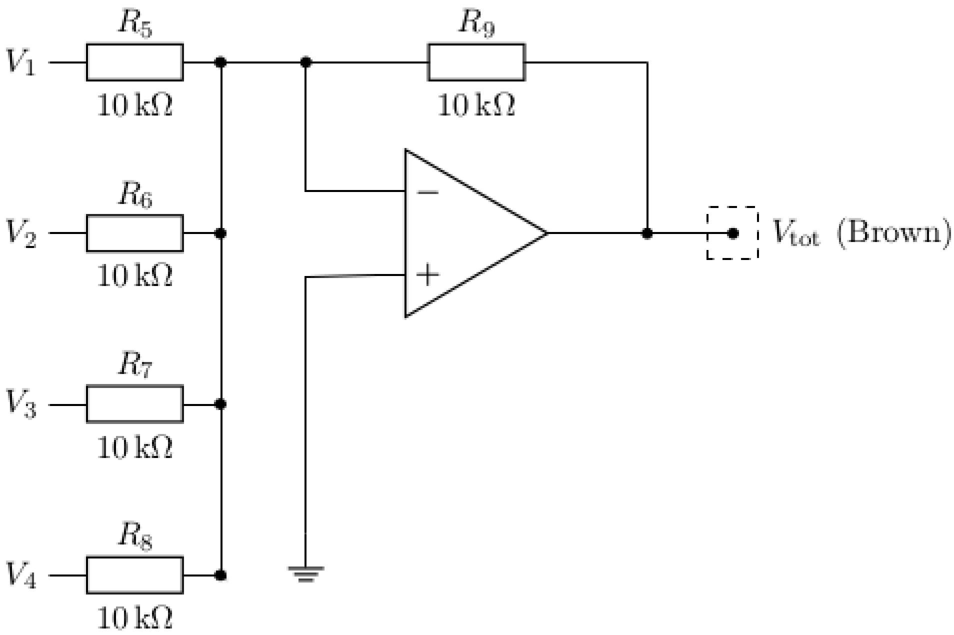

Figure 3.8: Circuit used to sum over the four photovoltages V_1, V_2, V_3, and V_4. The resistances $R_i = 10\,\mathrm{k}\Omega$ lead to a gain of one.

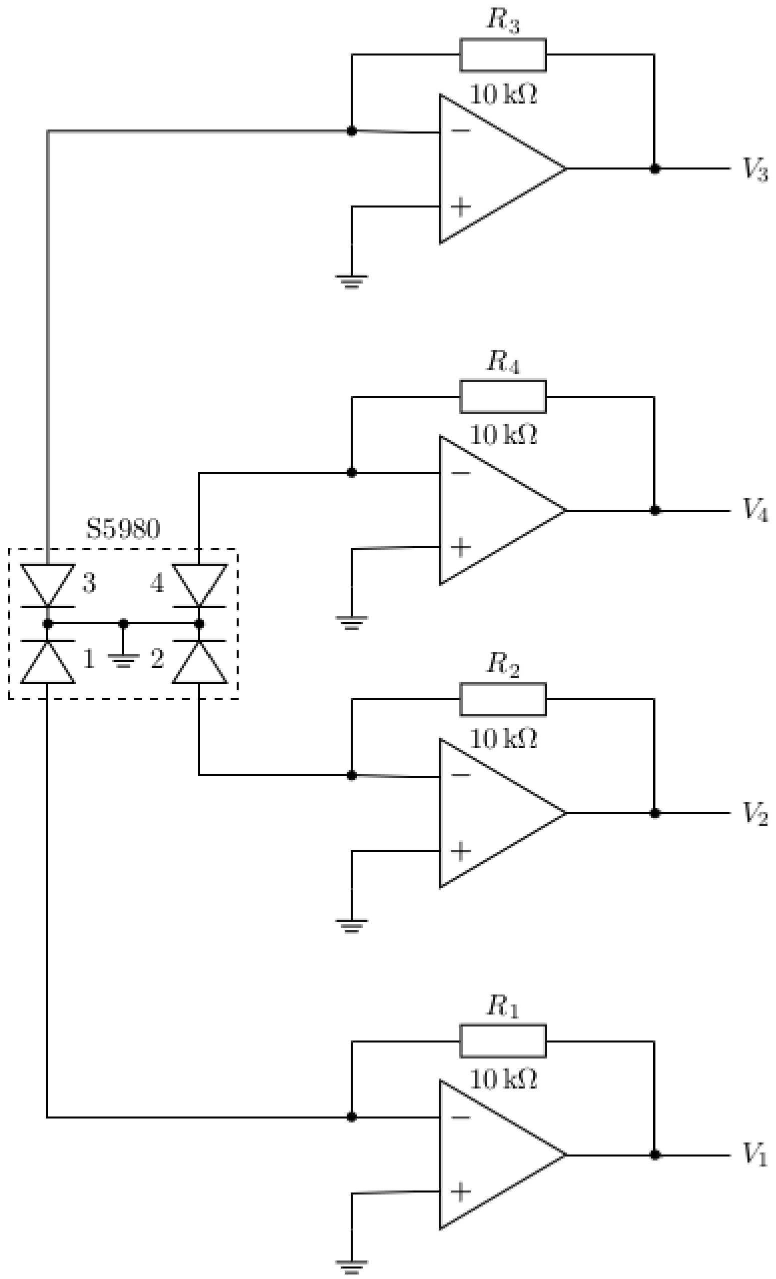

Figure 3.9: The four photo diodes, which comprise the quad segment diode are connected to individual transimpedance amplifiers which convert photocurrents into the voltages V_i. The voltages are given by $V_i = -I_{\text{photo}} \cdot 10\,\text{k}\Omega$.

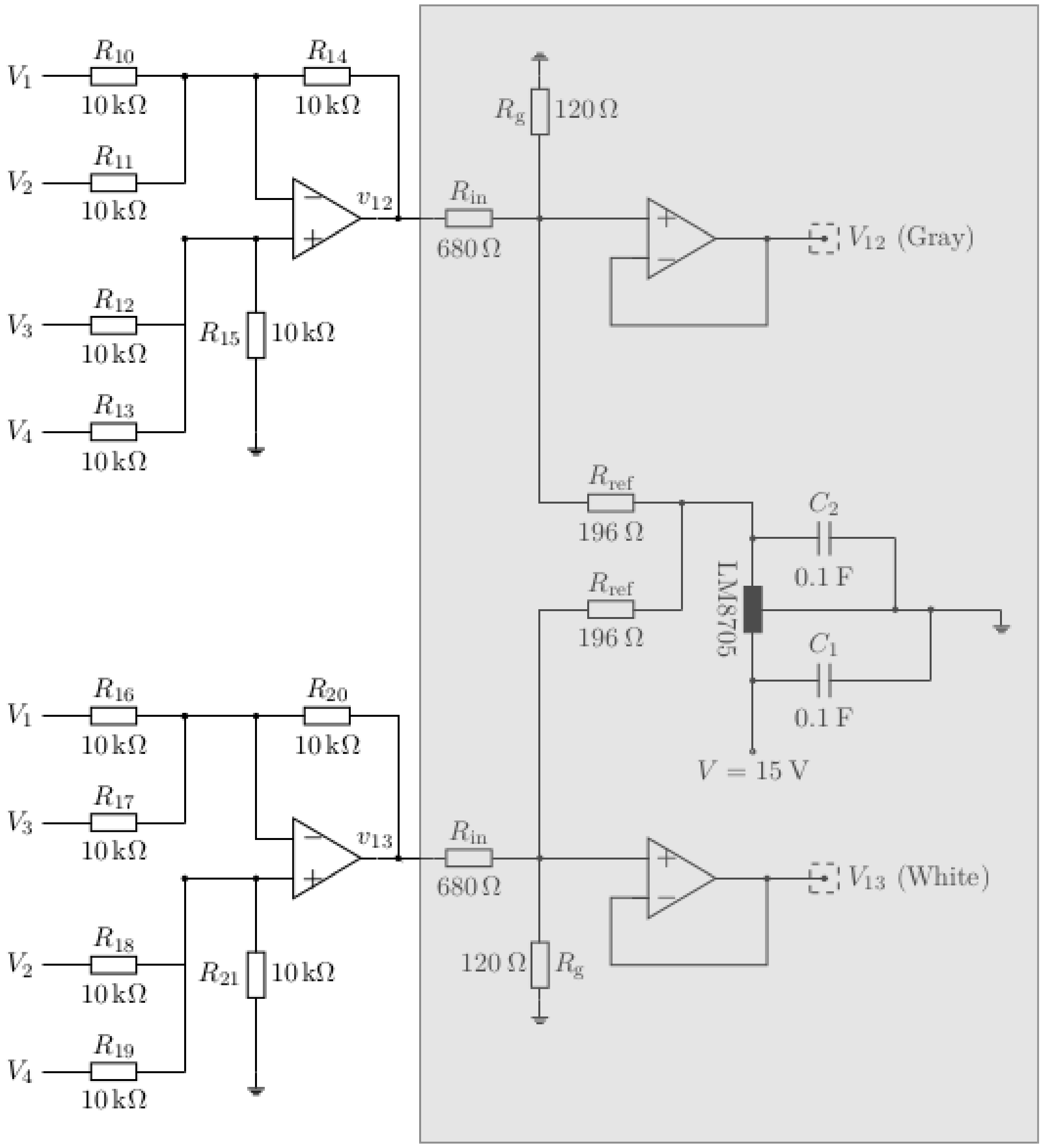

Figure 3.10: The converted voltages from each of the four photodiodes comprising the quad segment diode are funneled into op amp circuits which subtract off two of the four voltages enabling spatial resolveability. The output voltages v_{12} and v_{13} are then each fed into a circuit which provides a variable attenuation and DC-offset. The resistances R_{in}, R_{g}, and R_{ref} were chosen to provide the correct slope and y-intercept, and the capacitors provide stability to the 5 V voltage regulator producing the reference voltage for the circuit.

3.3 Automation of the Imaging Scheme

The automation of the self-correcting mirror is coordinated by means of an *Arduino* programm in addition to a *APT* parameter set to configure servo motor drivers. The parameter set configures the motor driver and motor actuators to be compatible with *Arduino* programm.

■ APT Software Parameter Set

The individual settings of the two servo motor controllers are configured using the *APTUser* utility. The user interface of the programm enables the setting of both motor controllers simultaneously and allows for the saving of a specific configuration as a parameter set. Before initiating the mirror correcting algorithm, a parameter set[13] must be loaded to the two motor drivers.[14] The parameter set configures the jog function with a 9 µm step size and removes the acceleration and deceleration between the steps. Furthermore, the homing mode for the actuators is configured with a homing position set in the forward direction with the foward limit switch. In addition, a homing *zero offset* of 0.9 mm was introduced. The *home* move is performed to establish a datum from which subsequent position moves can be measured [28]. This feature is necessary for the initialization of the *Arduino* programm so as to direct the laser beam to the lower right edge of the the first lens in the optical set-up L_1. This not only prevents the beam from straying unexpectadely from the optical set-up, but also minimizes the number of steps necessary during the scanning mode of the mirror correction programm. It is important to note that a homing move can also be performed by holding down both front panel buttons on the motor drivers for approximately two seconds. This becomes relevant for the intialization of the mirror correction programm.

■ Correction Algorithm

The correction algorithm used to correct the tilted mirror establishes three modes, the initialization, the scanning mode, and the precision positioning mode. The initialization procedure lasts 40 s and is used to define the so-called pin modes and perform a homing of the correcting mirror. A pin can be set to one of two pin modes, output or input. The output pin mode is used to supply voltage to whatever is connected to the pin, whereas the input pin mode is used to read external voltages. The four pins providing the voltage to the two servo motor drivers are set to output, and the three connections for the quad diode are set to input. The homing of the motors is realized by providing a LVTTL-signal from the four pins to the motors for four seconds.

The second mode of the programm is the scanning mode. During the main loop of the programm, the voltage readings originating from the quad diode are continously measured. If the total voltage V_{tot} from the total photovoltage connection at pin the respective pin is measured to be less than 0.3 V, then the motors are driven in such a way, so as to sweep the laser beam over the entire possible area in which the beam still passes through the optical set-up. Starting from the lower right bound of this area, the motor producing a left step is driven to the lower left bound of the area. After reaching the lower left bound of the correction area, the beam is directed upwards 20 steps before traversing the area

[13] The parameter set *mirror/correction*

[14] This is performed by loading up the *APTUser* utility, clicking on *View*, then *Graphical Panels*. The respective serial numbers of the two TDC001 motor drivers appear After the two graphical panels are open, the parameter set should be loaded automatically. If this is not the case, the parameter set may be manually loaded.

once more to the right. In between each step, the diode voltages are measured, and this S-shaped scanning pattern is performed until the reading from V_{tot} exeeds $0.3\,\mathrm{V}$, indicating that the beam has struck the photosensistive area of the segment diode.

If the laser beam strikes the quad photodiode at any point, the scanning mode is switched to the precision positioning mode. The photovoltages V_{12} and V_{13} read by the respective pins depend on the position of the beam on the photosensistive surface of the quad diode. If the beam is not in contact with the photosensitive surface or if the beam is centered inbetween each of the four diode elements comprising the diode, the voltages read $V_{12} = 1.72\,\mathrm{V}$ and $V_{13} = 1.72\,\mathrm{V}$. However, if the beam strikes the diode but is not centered ($V_{\mathrm{tot}} \geq 0.3\,\mathrm{V} \wedge V_{12} \neq 1.72\,\mathrm{V} \wedge V_{13} \neq 1.72\,\mathrm{V}$), then the motors are driven based on the voltage conditions defined by the programm. Each time through the loop the conditions are checked, and the motors are driven conversely to the conditions determined. For example, if the voltages measured fulfil the condition that the beam is located above and to the right of the center of the diode *UP RIGHT*, then the motors corresponding to the movements down and left are each driven one step before checking the condition once more. A full list of the voltage conditions defined by the programm as well as the voltage particular to the laser used in the test set-up are in table A.1. The centering procedure is continued until the voltages V_{12} and V_{13} are registered to be between $1.68\,\mathrm{V}$ and $1.75\,\mathrm{V}$. This tolerance threshold can be further restricted if the step size of the motors, configured with the APTUser utility is reduced. However, due to the length of the beam path to the quad diode and the fact that the degree of tilt of TM is unknown, lower step sizes correspond to longer scanning times during the scanning process.

Chapter 4

Characterisation of the Imaging Scheme

The imaging scheme presented in the previous chapter 3 is self-adjusting. The laser beam used to illuminate the atomic cloud below the ion microscope modifies its direction based on information received from a quadrant photodiode, and the movements of the laser beam are coordinated by a micro controller which drives the motorized actuators of a gimble mirror. The extent to which the optical and electronic configuration is able to correct for differing tilts of the mirror inside the ion microscope depends on the reliability of the quad segment photodiode, in conjunction with the employed electronics, as well as the tolerance threshold defined by the software. Furthermore, the consistency of the adjustment process for various degrees of tilt of the problematic mirror must be investigated.

4.1 Long Time Measurement of Zero Point Drift

Due to the circuits providing variable attenuation and DC-offsets to the output of the photodiode, shown in figure 3.10, a voltage drift over time could occur at the zero point. In turn, this voltage drift may cause the motorized mirror to adjust the direction of the beam even after it was successfuly centered. To investigate this possibility a long time measurement of the correction process was performed.

The output voltages of the photodiode (see figure 3.10) v_{12} and v_{13} have a voltage range ±15 V with the zero point being at 0 V. These voltages were then mapped onto the compatible range of voltages for the micro controller (0 V – 3.3 V) which, subsequently, leads to a shift of the zero point to 1.72 V for both outputs. Because the y-intercept of the output voltage function is no longer at zero, and the fact that additional circuitry was introduced into the configuration, could lead to the appearance of a voltage drift. The correction algorithm continuously measures the voltages originating from the photodiode in order to update the conditions used to drive the motor mirror. If, after the centering of the beam, a voltage drift exeeding the voltage range defined by the tolerance threshold exists, then the programm will attempt to correct for the fictitious shift of the laser on the diode.

In order to investigate the voltage drift possibility, a long time measurement of the correction process was performed. Through the use of the optical configuration typified in figure 4.2, the laser beam at the position of the atomic cloud in the vacuum chamber can be imaged onto a CCD camera. After the beam passes the lens L_3 with the working distance of the relatively flat surface $f_3^{fl} = 21\,\mathrm{mm}$, a 50/50 beam splitter is installed to deflect half of the intensity of the light in the direction of the fixed 2 inch dielectric mirror FM5. The beam is then directed to the CCD camera. To mimic the position of the atomic cloud imaged inside the ion microscope, a needle was placed 10 mm from the pinhole PH and 21 mm from L_3. With the placement of the lens L_6 with focal length $f_6 = 50$ mm, an image of the needle appears 50 mm away from L_6 towards FM5. This image becomes the object for the rest of the optical path. The lenses L_7 and L_8 with focal lengths $f_7 = 200$ mm and $f_8 = 50$ mm then image the beam at the focal point of L_8. The image of the needle is sharp when the optical components, especially L_7 and L_8 are properly positioned. With this configuration, the movement of the beam resulting from the self-adjustment process can be imaged, and because this movement occurs in the same manner at both the position of the CCD camera and the position of photodiode, the trajectory of the laser striking the diode is able to be monitored.

For the long time measurement, the correction algorithm was executed, and the laser was centered. At this point a snapshot of the beam position on the CCD camera was taken every minute for a total of 480 minutes. The position on the camera was determined by fitting a Gaussian profile to the image[1]. This measurement was performed during the day, enabling the incorporation of the largest temperature fluctuations which may also perturb the characteristics of the electronic components. Figure 4.1 is a plot of the position of the beam relative to the mean position ($x = 2128\,\mu$m and $y = 1356\,\mu$m) in intervals of 15 minutes for a total of 480 minutes. The position of the beam did not markedly fluctuate, with a beam drift in the x- and y-direction being predominantly less than $\pm 10\,\mu$m and maximaly less $\pm 20\,\mu$m. For the sake of clarity, only the 95 % confidence bounds of the fit for one data point at the 15 minute mark were plotted in figure 4.1. However, all points were of similar magnitude, such that no significant displacement during the eight hour measurement could be detected.

[1]The pixel size was assumed to be approximately $2.79\,\mu$m

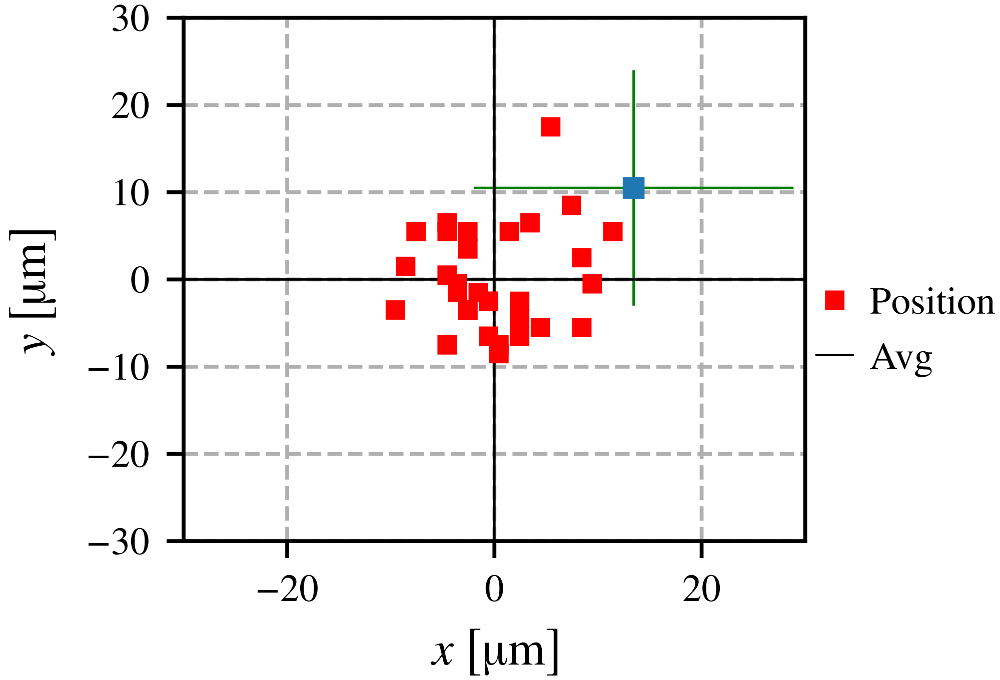

Figure 4.1: Plot of the fluctuations Δx and Δy of the beam in intervals of 15 minutes for 480 minutes relative to the mean position of the beam $x = 2128\,\mu\text{m}$ and $y = 1356\,\mu\text{m}$. The deviations at the position of the atoms did not exceed $\pm 20\,\mu\text{m}$ with the largest portion of positions being within $\pm 10\,\mu\text{m}$. The typical confidence bounds of the fit are shown for the one point at the 15 minute mark, indicated in blue.

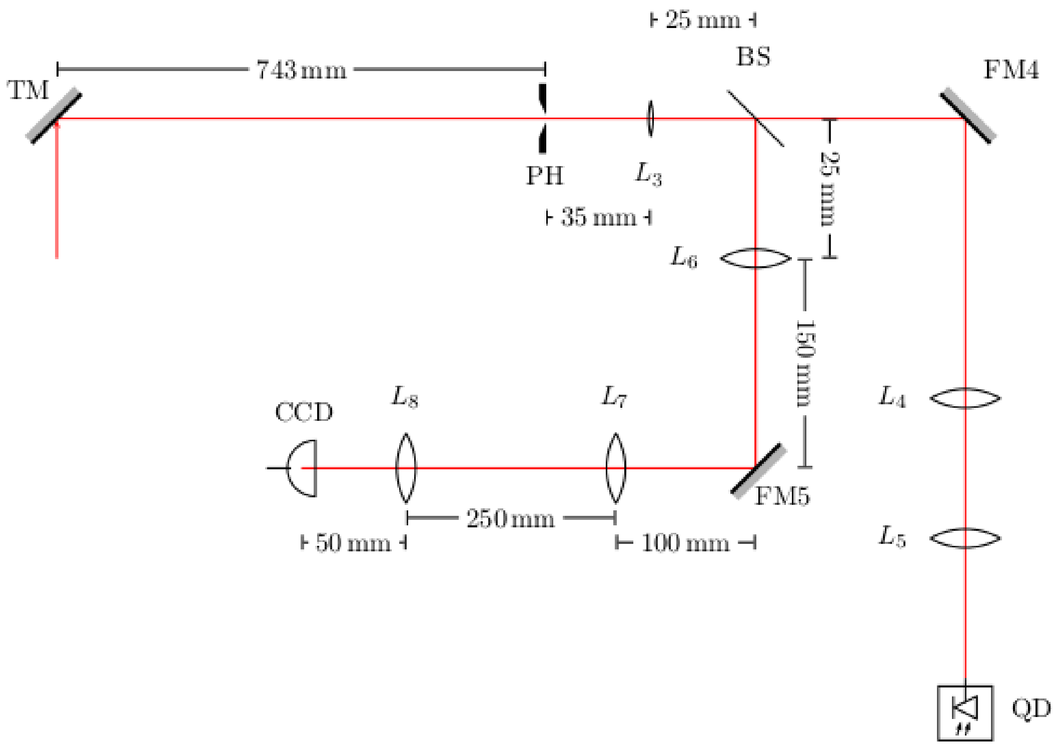

Figure 4.2: Installment of the CCD camera in order to indirectly monitor the position of the beam on the photodiode QD. The beam splitter funnels half of the laser intensity in the direction of the fixed dielectric mirror FM5. Lens L_6 has a focal length of $f_6 = 50\,\mathrm{mm}$ and lenses L_7 and L_8 have focal lengths $f_7 = 200\,\mathrm{mm}$ and $f_8 = 50\,\mathrm{mm}$ respectively.

4.2 Mirror Correction Fidelity

After determining the extent of voltage drift, the fidelity of the self-adjustment process can be investigated using the same set-up in figure 4.2. Not only is it important to test the correction process for various mirror tilts, but it is also important to determine the consistency of the position of the beam at the position of the atoms after the correction takes place. Because the software allows for a certain tolerance of the targeted voltages, the beam position after correction could vary from programm execution to programm execution. This does not pose a problem if the variance with respect to a perfectly centered beam remains minimal.

In order to orient the optical components correctly so as to enable the most central beam path through the entire optical set-up, the lenses L_1 and L_2 in figure 3.3 were outfitted with aperatures. The laser was then directed through the center of the lenses by manually adjusting the self-adjusting mirror SAM. Furthermore, the tilted mirror TM was straightened so that the beam would strike the photodiode centrally. An image of the beam on the CCD camera was then taken, and the image was fitted with a Gaussian profile to calculate the position of the central point $x_0 = 2321\,\mu\text{m}$ and $y_0 = 1615\,\mu\text{m}$. Afterwards, the correction process was repeated five times for the various mirror tilts α^x and α^y of TM. The distance away from x_0 and y_0 was calculated and plotted for the mirror tilts $\alpha^x = \alpha^y = 0.0°$, $\alpha^x = \alpha^y = 0.5°$, $\alpha^x = \alpha^y = 1.0°$, and $\alpha^x = \alpha^y = 1.5°$. Figure 4.3 represents the results.

Initially, in the absence of a mirror tilt, x_0 and y_0 remained within $\pm 40\,\mu\text{m}$ and $\pm 20\,\mu\text{m}$ respectively. As soon as the mirror tilt was set to $\alpha^x = \alpha^y = 0.5°$, however, $x_{0.5}$ and $y_{0.5}$ noteably increased. The distances $x_{1.5}$ and $y_{1.5}$ are shown in figure 4.3d. The deviations of the beam with a mirror tilt of $\alpha^x = \alpha^y = 1.5°$, congregated in one quadrant and the typical deviations of the beam for all mirror tilts remained within 200 µm, with a significant portion remaining within 100 µm. Furthermore, it is also important to note that the overall position with increasing mirror tilt in the positive x and y direction indicated a trend to one quadrant, exhibited in figure 4.3. This indicates a systematic error which could have been introduced, for example, through spherical aberration of the lenses or suboptimal lens distances. Apart from systematic effects, a minimization of the encountered error could be achieved by reducing the step size of the motors and reducing the tolerance threshold in the correction algorithm. However, if the range is configured too restrictively, then the 9 µm motor step size may become too large for the center of the photosensitive area of the diode due to the extensive distance the beam travels through the apparatus. If the step of the laser in the direction of the center of the diode is too large, then the programm must correct by stepping in the converse direction. If, however, the correction step is once again too large, then the beam will remain in a perpetual correction process. If this is a problem, the motor step size can be further reduced at the expense of a longer correction duration.

Due to the fact that the magnification of the beam at the position of the atomic cloud is twice as large as the image on the CCD camera, the deviations measured in figure 4.3 are twice as large at the position of the atomic cloud. For example, a deviation of 100 µm corresponds to a displacement of the beam at the position of the atoms of 200 µm. This may pose a problem for the more significant deviations measured. However, the size of the laser beam is approximately 2 mm, and the typical displacements measured at the position of atoms ranged from (300 µm - 400 µm). Therefore, the deviations observed are not as significant. In order to improve the consistency of the laser beam corrections, a combination of a smaller step size and a reduction of the tolerance threshold should be attempted.

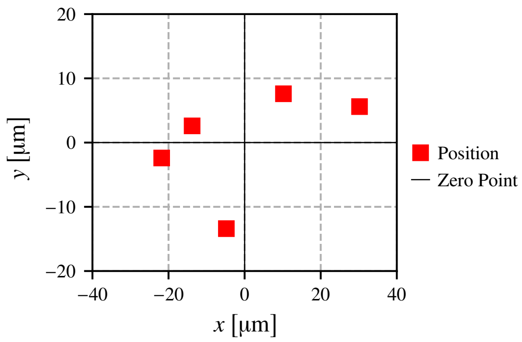

(a) Correction of mirror without tilt $\alpha^x = \alpha^y = 0.0°$.

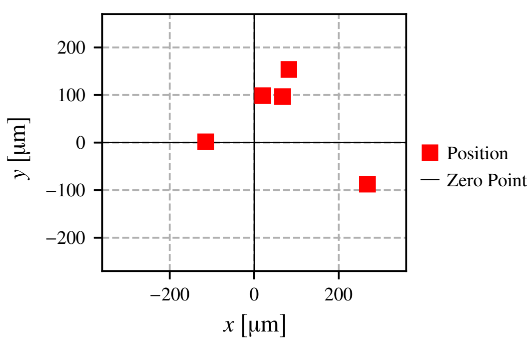

(b) Correction of mirror with tilt $\alpha^x = \alpha^y = 0.5°$.

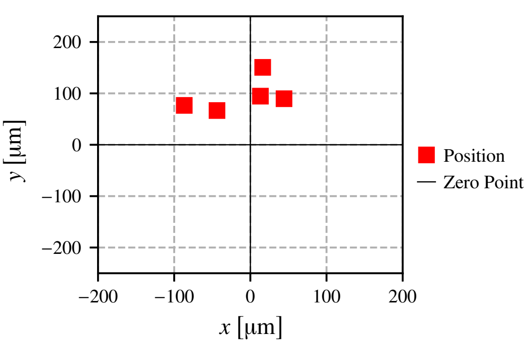

(c) Correction of mirror with tilt $\alpha^x = \alpha^y = 1.0°$.

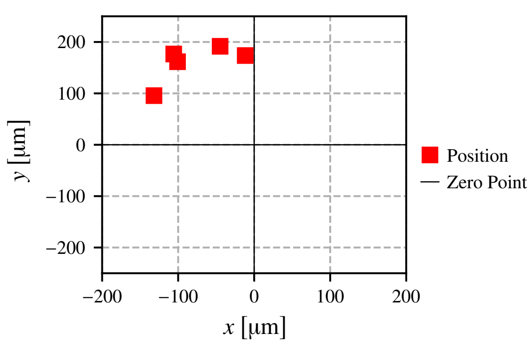

(d) Correction of mirror with tilt $\alpha^x = \alpha^y = 1.5°$.

Figure 4.3: Results of the mirror correction process for differing tilt angles of the in-vacuum mirror. The correction process was performed five times for each degree of tilt, and the distance away from the central point $x_0 = 2321\,\mu m$ and $y_0 = 1615\,\mu m$, represented by the black horizontal and vertical lines at the origin, is plotted (red squares). The fluctuation of the position of the beam after each attempt for all degrees of tilt typically remained within $\pm 200\,\mu m$ for both x and y, with a significant portion of the attempts remaining within $\pm 100\,\mu m$.

4.3 Trajectory of the Beam on the Photodiode

In order to illustrate the precision positioning mode performed when the laser strikes the photodiode, a video was taken during the centering process with the CCD camera. By determining the position of the beam in each frame, a plot of the beam trajectory was constructed, and the results are displayed in figure 4.4. The beam was registered at the edge of the photosensistive surface by the diode. The condition, based on the voltages read, dictated the proper driving of the mirror to direct the beam to the center. Figure 4.5 shows the images of the beam from the CCD camera during the correction process.

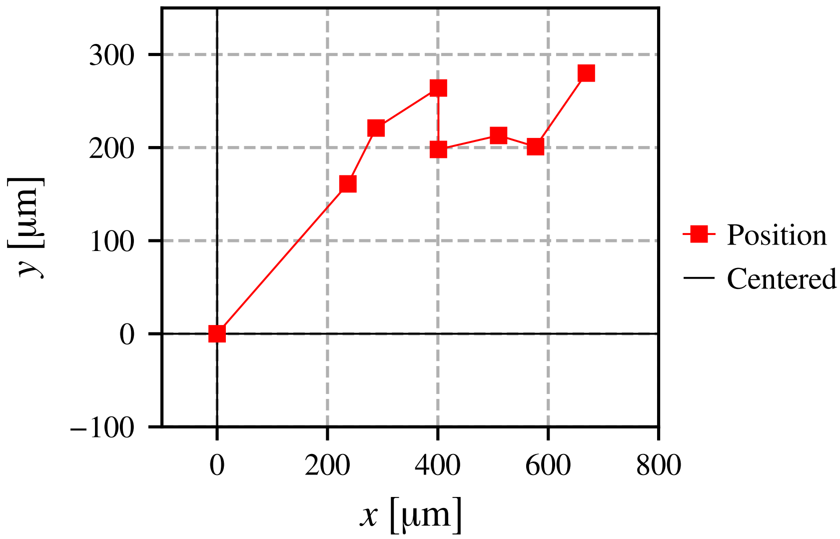

Figure 4.4: Trajectory of the beam during the centering process. The distances are relative to the point at which the beam is center, given by the origin. The photodiode sensed the beam near the edge of the photosensistive area before initializing the precision motor steps.

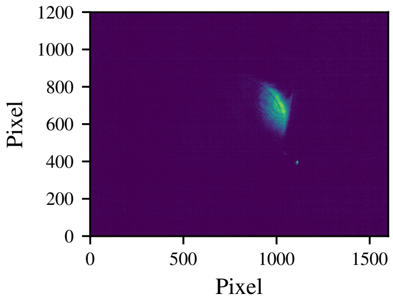

(a) Step 1

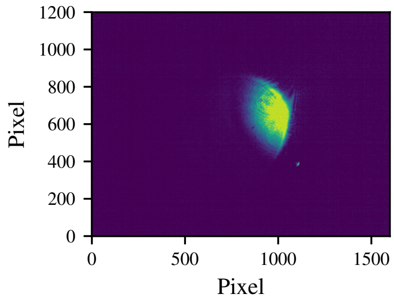

(b) Step 2

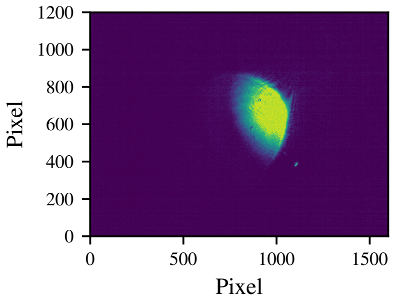

(c) Step 3

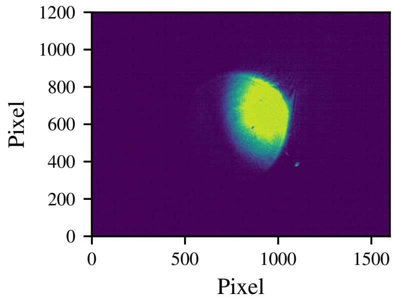

(d) Step 4

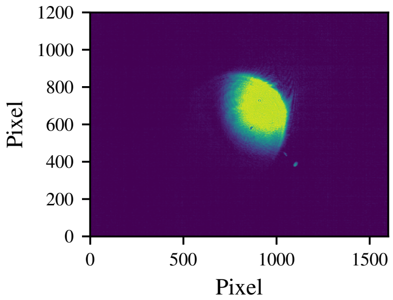

(e) Step 5

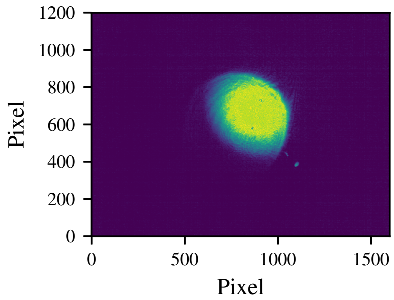

(f) Step 6

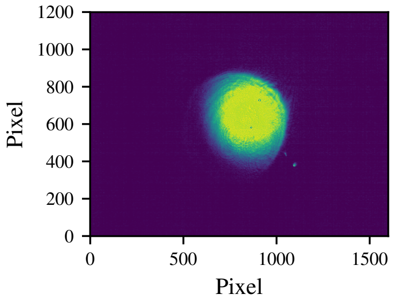

(g) Step 7

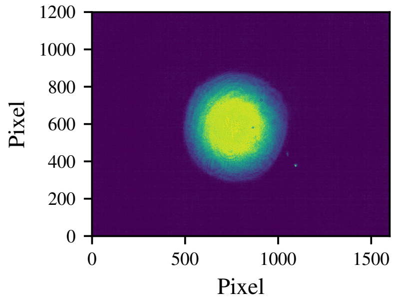

(h) Step 8

Figure 4.5: Path taken by beam during the centering process.

Chapter 5

Summary and Outlook

Within the scope of this thesis, an absorption imaging scheme was developed for deployment on ultracold atomic physics experiments with an ion microscope. As the detector of the ion microscope makes it impossible to shoot an imaging beam directly to the atoms, a moveable in-vacuum mirror is installed to deflect the imaging light through the microscope. This mirror, however, exhibits a slightly inconsisent tilt which manifests itself over multiple experimental attempts. Therefore, the imaging scheme was designed to be self-adjusting and was accomplished by implementing two plano-convex lenses in a telescopic configuration. The laser beam traverses the optical path of the set-up and centrally strikes the in-vacuum mirror. By utilizing a gimble mount housing a 1 inch dielectric mirror and installing motorized actuators driven by servo motor controllers, the direction of the laser beam can be altered in such a way so as to vary the angle of incidence of the beam onto the mirror. This, in turn, modifies the angle of reflection off of the tilted mirror. This way, the beam path through the ion microscope can be corrected, irregardless of the degree of tilt. In order to automate the adjustment process, a micro controller was implemented which enables the coordination of the motorized actuators with respect to the information garnered from a quad segment photodiode.

In order to characterize the self-adjustment process, the mirror correction software was executed for various degrees of tilt of a mirror which mimicked the in-vacuum mirror inside the ion microscope. The beam at the position where the atomic cloud would be located was imaged onto a CCD camera, and with this set-up, the movement of the beam on the photodiode could be indirectly monitored. In all instances of the programm, the tilts of the mirror between the $0°$ and $1.5°$ were corrected, with typical horizontal and vertical deviations at the position of the atoms being within (200 µm - 400 µm). Moreover, due to the fact that two of the outputs of the photodiode required the implementation of a circuit which provided a DC-offset away from the zero point, the question arose, to what extent the additional circuitry leads to a drift of the zero point. This is relevant because, the correction algorithm continously measures the voltages from the diode, and if the voltages differ over time, this could cause the beam on the photosensitive area of the diode to fluctuate. To investigate this possibility the mirror correction programm was run, and the tilt of the mirror was corrected at which point a snapshot of the beam was taken every 60 seconds for a total of eight hours. The measured beam positions indicated fluctuations which did not exceed 20 µm in both orientations. If, however, the 95 % confidence bounds of the fits used to determine the positions of the beam are considered, then it can be concluded that the laser beam position did not fluctuate to any significant extent.

In the near future, the self-adjusting imaging scheme will be deployed on the ion microscope. This will provide transversal imaging possibilities which seemlessly integrate into the rest of the automized experimental protocol. Furthermore, the imaging scheme will be able to recognize whether the atoms are properly positioned below the microscope, and in the far future, a novel method for probing ion-atom collisions in the ultracold quantum regime through exploitation of the characteristics of Rydberg molecules will be attempted. [8]

Appendix A

Appendix

A.1 The Imaging Scheme

The four female BNC connections of the motor drivers are connected to the pins D14 (DOWN), D17 (UP), D20 (LEFT), and D23 (RIGHT) which are shown in figure 3.5 by means of BNC male connectors drilled into the metal casing housing the micro controller. The ground of the individual male connectors is then connected to the collector end of the transistors in figure 3.6 while the signal carrying center core is soldered to the cable providing the 5 V powering the *Teensy 3.2*. The motor driver coressponding to the movements up and down is the TDC001 with serial number 83825807, and the TDC001 with serial number 83827882 is responsible for the motor movements left and right. Figure A.1.

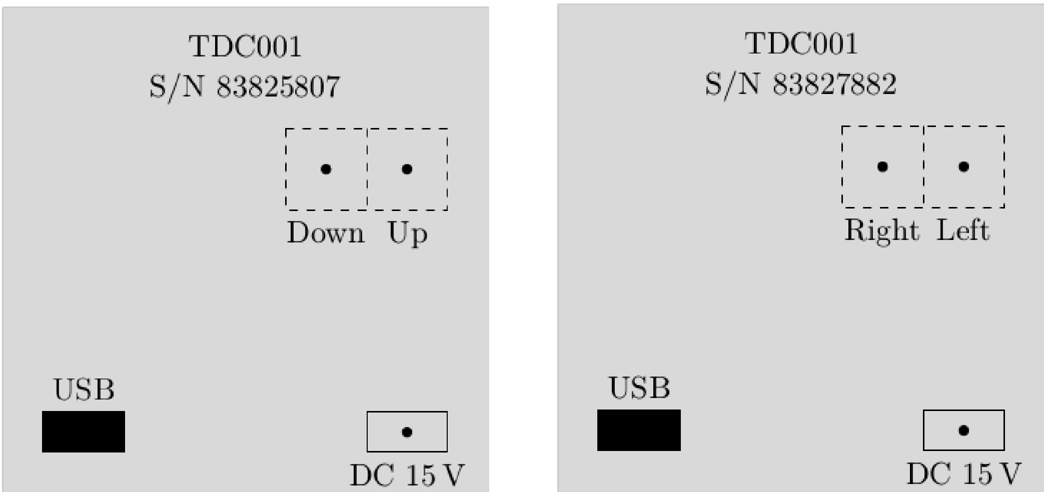

(a) Mirror movements up and down. **(b)** Mirror movements to the right and left.

Figure A.1: For consistency with the *Arduino* programm, The rear panel of the two servo motor drivers with BNC marked BNC connections are distinguished.

A.2 Automation of the Imaging Scheme

Table A.1: The position of the beam on the photodiode determined by the voltage conditions for V_{tot}, V_{12}, and V_{13} in the particular set-up. These voltages may differ depending on the laser powers present. If the beam is not incident on the surface of the photodiode, then the condition INVALID is true.

Position	Voltage Condition
CENTERED	$(V_{\text{tot}} \geq 0.3\,\text{V}) \wedge (V_{12} \geq 1.68\,\text{V} \wedge V_{12} \leq 1.75\,\text{V}) \wedge (V_{13} \geq 1.68\,\text{V} \wedge V_{13} \leq 1.75\,\text{V})$
ABOVE	$(V_{\text{tot}} \geq 0.3\,\text{V}) \wedge (V_{12} < 1.68\,\text{V}) \wedge (V_{13} \geq 1.68\,\text{V} \wedge V_{13} \leq 1.75\,\text{V})$
BELOW	$(V_{\text{tot}} \geq 0.3\,\text{V}) \wedge (V_{12} > 1.75\,\text{V}) \wedge (V_{13} \geq 1.68\,\text{V} \wedge V_{13} \leq 1.75\,\text{V})$
LEFT	$(V_{\text{tot}} \geq 0.3\,\text{V}) \wedge (V_{13} > 1.75\,\text{V}) \wedge (V_{12} \geq 1.68\,\text{V} \wedge V_{12} \leq 1.75\,\text{V})$
RIGHT	$(V_{\text{tot}} \geq 0.3\,\text{V}) \wedge (V_{13} < 1.68\,\text{V}) \wedge (V_{12} \geq 1.68\,\text{V} \wedge V_{12} \leq 1.75\,\text{V})$
ABOVE RIGHT	$(V_{\text{tot}} \geq 0.3\,\text{V}) \wedge (V_{12} < 1.68\,\text{V}) \wedge (V_{13} < 1.68\,\text{V})$
ABOVE LEFT	$(V_{\text{tot}} \geq 0.3\,\text{V}) \wedge (V_{12} > 1.75\,\text{V}) \wedge (V_{13} > 1.75\,\text{V})$
BELOW RIGHT	$(V_{\text{tot}} \geq 0.3\,\text{V}) \wedge (V_{12} > 1.75\,\text{V}) \wedge (V_{13} < 1.68\,\text{V})$
BELOW LEFT	$(V_{\text{tot}} \geq 0.3\,\text{V}) \wedge (V_{12} > 1.75\,\text{V}) \wedge (V_{13} > 1.75\,\text{V})$
INVALID	$V_{\text{tot}} < 0.3\,\text{V}$

Bibliography

[1] Daniel Adam Steck. “Rubidium 87 D Line Data.” In: (Jan. 2003).

[2] M. H. Anderson et al. “Observation of Bose-Einstein Condensation in a Dilute Atomic Vapor.” In: *Science* 269.5221 (1995), pp. 198–201. ISSN: 0036-8075. DOI: 10.1126/science.269.5221.198. eprint: https://science.sciencemag.org/content/269/5221/198.full.pdf. URL: https://science.sciencemag.org/content/269/5221/198.

[3] Bose. “Plancks Gesetz und Lichtquantenhypothese.” In: *Zeitschrift fur Physik* 26 (Dec. 1924), pp. 178–181. DOI: 10.1007/BF01327326.

[4] C. C. Bradley et al. “Evidence of Bose-Einstein Condensation in an Atomic Gas with Attractive Interactions.” In: *Phys. Rev. Lett.* 75 (9 1995), pp. 1687–1690. DOI: 10.1103/PhysRevLett.75.1687. URL: https://link.aps.org/doi/10.1103/PhysRevLett.75.1687.

[5] K. B. Davis et al. “Bose-Einstein Condensation in a Gas of Sodium Atoms.” In: *Phys. Rev. Lett.* 75 (22 1995), pp. 3969–3973. DOI: 10.1103/PhysRevLett.75.3969. URL: https://link.aps.org/doi/10.1103/PhysRevLett.75.3969.

[6] W. Demtröder. *Experimentalphysik 2*. Experimentalphysik / Wolfgang Demtröder. Springer Berlin Heidelberg, 2008. ISBN: 9783540682196. URL: https://books.google.de/books?id=AtDxWU39CTMC.

[7] Christopher J Foot. *Atomic physics*. Oxford master series in atomic, optical and laser physics. Oxford: Oxford University Press, 2007. URL: https://cds.cern.ch/record/1080846.

[8] Sergio Franco. 3rd ed. New York, NY, USA: McGraw-Hill, Inc., 2002. ISBN: 0072320842, 9780072320848.

[9] Yu Gnedin et al. “Rydberg atoms in astrophysics.” In: *New Astronomy Reviews* 53 (Aug. 2009), pp. 259–265. DOI: 10.1016/j.newar.2009.07.003.

[10] Axel Rudolf Griesmaier. “Dipole-dipole interaction in a degenerate quantum gas.” PhD thesis. University of Stuttgart, 2006.

[11] H. Häberlin. *Photovoltaics: System Design and Practice*. Wiley, 2012. ISBN: 9781119978381. URL: https://books.google.de/books?id=w8k3aXBnDP4C.

[12] P. Horowitz and W. Hill. *The Art of Electronics*. Cambridge University Press, 2015. ISBN: 9780521809269. URL: https://books.google.de/books?id=LAiWPwAACAAJ.

[13] R. B. Hurley. “The Role of Transistors in Electronics.” In: *Journal of the SMPTE* 66.6 (1957), pp. 330–332. ISSN: 0361-4573. DOI: 10.5594/J11233.

[14] F. London. “The -Phenomenon of Liquid Helium and the Bose-Einstein Degeneracy.” In: *Nature* 141.3571 (Apr. 1938), pp. 643–644. ISSN: 0028-0836. DOI: 10.1038/141643a0. URL: http://dx.doi.org/10.1038/141643a0.

[15] Ron Mancini. *Op Amps For Everyone*. Texas Instruments, 2002.

[16] Ron Mancini. *Understanding Basic Analog – Ideal Op Amps*. Texas Instruments, 2016.

[17] Alan L. Migdall et al. “First Observation of Magnetically Trapped Neutral Atoms.” In: *Phys. Rev. Lett.* 54 (24 1985), pp. 2596–2599. DOI: 10.1103/PhysRevLett.54.2596. URL: https://link.aps.org/doi/10.1103/PhysRevLett.54.2596.

[18] NobelPrize.org. *The Nobel Prize in Physics 1997*. 1997. URL: https://www.nobelprize.org/prizes/physics/1997/9955-the-nobel-prize-in-physics-1997/ (visited on 09/01/2019).

[19] NobelPrize.org. *The Nobel Prize in Physics 2001*. 2001. URL: https://www.nobelprize.org/prizes/physics/2001/summary/ (visited on 09/01/2019).

[20] A. Osterwalder and F. Merkt. “Using High Rydberg States as Electric Field Sensors.” In: *Phys. Rev. Lett.* 82 (9 1999), pp. 1831–1834. DOI: 10.1103/PhysRevLett.82.1831. URL: https://link.aps.org/doi/10.1103/PhysRevLett.82.1831.

[21] PJRC. *Teensy 3.2/3.1*. URL: https://www.pjrc.com/teensy/teensy31.html (visited on 09/01/2019).

[22] Enric Pérez and Tilman Sauer. “Einstein’s quantum theory of the monatomic ideal gas: Non-statistical arguments for a new statistics.” In: *Archive for History of Exact Sciences* 64 (Sept. 2010), pp. 561–612. DOI: 10.1007/s00407-010-0066-x.

[23] Bahaa E A Saleh and Malvin Carl Teich. *Fundamentals of photonics; 2nd ed.* Wiley series in pure and applied optics. New York, NY: Wiley, 2007. URL: https://cds.cern.ch/record/1084451.

[24] W. Schmusch. *Elektronische Meßtechnik: Prinzipien, Verfahren, Schaltungen*. Vogel, 1993. ISBN: 9783802314940. URL: https://books.google.de/books?id=y_Y1NgAACAAJ.

[25] J. A. Sedlacek et al. “Atom-Based Vector Microwave Electrometry Using Rubidium Rydberg Atoms in a Vapor Cell.” In: *Phys. Rev. Lett.* 111 (6 2013), p. 063001. DOI: 10.1103/PhysRevLett.111.063001. URL: https://link.aps.org/doi/10.1103/PhysRevLett.111.063001.

[26] *Si PIN photodiodes S5980, S5981,S5870*. HAMAMATSU. 2018.

[27] David A. Smith et al. “Absorption imaging of ultracold atoms on atom chips.” In: *Opt. Express* 19.9 (2011), pp. 8471–8485. DOI: 10.1364/OE.19.008471. URL: http://www.opticsexpress.org/abstract.cfm?URI=oe-19-9-8471.

[28] *TDC001 DC Servo Motor Driver*. Thorlabs.

[29] A. Urvoy et al. “Strongly Correlated Growth of Rydberg Aggregates in a Vapor Cell.” In: *Phys. Rev. Lett.* 114 (20 2015), p. 203002. DOI: 10.1103/PhysRevLett.114.203002. URL: https://link.aps.org/doi/10.1103/PhysRevLett.114.203002.

[30] Nikola Šibalić and Charles S Adams. *Rydberg Physics*. 2399-2891. IOP Publishing, 2018. ISBN: 978-0-7503-1635-4. DOI: 10.1088/978-0-7503-1635-4. URL: http://dx.doi.org/10.1088/978-0-7503-1635-4.